



Analysis of the full Spitzer microlensing sample I: Dark remnant candidates and Gaia predictions

KRZYSZTOF A. RYBICKI ¹, YOSSI SHVARTZVALD,¹ JENNIFER C. YEE,² SEBASTIANO CALCHI NOVATI,³ ERAN O. OFEK,¹
IAN A. BOND,⁴

















(LEADING AUTHORS)

CHARLES BEICHMAN,³ GEOFF BRYDEN,³ SEAN CAREY,³ CALEN HENDERSON,³ WEI ZHU,⁵ MICHAEL M. FAUSNAUGH ⁶,
BENJAMIN WIBKING,⁷


(THE SPITZER TEAM)

ANDRZEJ UDALSKI,⁸ RADEK POLESKI,⁸ PRZEMEK MRÓZ,⁸ MICHAŁ K. SZYMAŃSKI,⁸ IGOR SOSZYŃSKI,⁸
PAWEŁ PIETRUKOWICZ,⁸ SZYMON KOZŁOWSKI,⁸ JAN SKOWRON,⁸ KRZYSZTOF ULACZYK,^{9,8} PATRYK IWANEK,⁸
MARCIN WRONA,⁸

(THE OGLE COLLABORATION)

YOON-HYUN RYU ¹⁰, MICHAEL D. ALBROW ¹¹, SUN-JU CHUNG ¹⁰, ANDREW GOULD,^{12,13} CHEONGHO HAN ¹⁴,
KYU-HA HWANG ¹⁰, YOUN KIL JUNG ^{10,15}, IN-GU SHIN ¹⁶, HONGJING YANG ¹⁷, WEICHENG ZANG ¹⁶,
SANG-MOK CHA ^{10,18}, DONG-JIN KIM,¹⁰ HYOUN-WOO KIM,¹⁰ SEUNG-LEE KIM ¹⁰, CHUNG-UK LEE ¹⁰,
DONG-JOO LEE ¹⁰, YONGSEOK LEE ^{10,18}, BYEONG-GON PARK ¹⁰, RICHARD W. POGGE ^{19,20}

(THE KMTNET COLLABORATION)

FUMIO ABE,²¹ RICHARD BARRY,²² DAVID P. BENNETT,^{22,23} APARNA BHATTACHARYA,^{22,23} AKIHIKO FUKUI,^{24,25}
RYUSEI HAMADA,²⁶ SHUNYA HAMADA,²⁶ NAOTO HAMASAKI,²⁶ YUKI HIRAO,²⁷ STELA ISHITANI SILVA,^{28,22}
YOSHITAKA ITOW,²¹ RINTARO KIRIKAWA,²⁶ NAOKI KOSHIMOTO,²⁶ YUTAKA MATSUBARA,²¹ SHOTA MIYAZAKI,²⁹
YASUSHI MURAKI,²¹ TUTUMI NAGAI,²⁶ KANSUKE NUNOTA,²⁶ GREG OLMSCHENK,²² CLEMENT RANC,³⁰
NICHOLAS J. RATTENBURY,³¹ YUKI K. SATOH ³², TAKAHIRO SUMI,²⁶ DAISUKE SUZUKI,²⁶ PAUL . J. TRISTRAM,³³
AIKATERINI VANDOROU,^{22,23} HIBIKI YAMA,²⁶

(MOA COLLABORATION)

LUKASZ WYRZYKOWSKI,⁸ KORNEL HOWIL,⁸ KATARZYNA KRUSZYŃSKA,³⁴

¹Department of Particle Physics and Astrophysics, Weizmann Institute of Science, Rehovot 76100, Israel

²Center for Astrophysics | Harvard & Smithsonian, 60 Garden St, MS-15 Cambridge, MA 02138, USA

³IPAC, Mail Code 100-22, Caltech, 1200 E. California Blvd., Pasadena, CA 91125, USA

⁴Institute of Natural and Mathematical Sciences, Massey University, Auckland 0745, New Zealand

⁵Department of Astronomy, Tsinghua University, Beijing 10084, China

⁶Department of Physics & Astronomy, Texas Tech University, Lubbock TX, 79410-1051, USA

⁷Michigan State University, 426 Auditorium Road East Lansing, MI 48824, USA

⁸Astronomical Observatory, University of Warsaw, Al. Ujazdowskie 4, 00-478, Warszawa, Poland

⁹Department of Physics, University of Warwick, Coventry CV4 7 AL, UK

¹⁰Korea Astronomy and Space Science Institute, Daejeon 34055, Republic of Korea

¹¹University of Canterbury, School of Physical and Chemical Sciences, Private Bag 4800, Christchurch 8020, New Zealand

¹²Max-Planck-Institute for Astronomy, Königstuhl 17, 69117 Heidelberg, Germany

¹³Department of Astronomy, Ohio State University, 140 W. 18th Ave., Columbus, OH 43210, USA

¹⁴Department of Physics, Chungbuk National University, Cheongju 28644, Republic of Korea

¹⁵National University of Science and Technology (UST), Daejeon 34113, Republic of Korea

¹⁶Center for Astrophysics | Harvard & Smithsonian, 60 Garden St., Cambridge, MA 02138, USA

¹⁷Department of Astronomy, Tsinghua University, Beijing 100084, China

¹⁸School of Space Research, Kyung Hee University, Yongin, Gyeonggi 17104, Republic of Korea

¹⁹Department of Astronomy, Ohio State University, 140 West 18th Ave., Columbus, OH 43210, USA

²⁰Center for Cosmology and AstroParticle Physics, Ohio State University, 191 West Woodruff Ave., Columbus, OH 43210, USA

²¹Institute for Space-Earth Environmental Research, Nagoya University, Nagoya 464-8601, Japan

²²Code 667, NASA Goddard Space Flight Center, Greenbelt, MD 20771, USA

²³Department of Astronomy, University of Maryland, College Park, MD 20742, USA

²⁴*Department of Earth and Planetary Science, Graduate School of Science, The University of Tokyo, 7-3-1 Hongo, Bunkyo-ku, Tokyo 113-0033, Japan*

²⁵*Instituto de Astrofísica de Canarias, Via Lactea s/n, E-38205 La Laguna, Tenerife, Spain*

²⁶*Department of Earth and Space Science, Graduate School of Science, Osaka University, Toyonaka, Osaka 560-0043, Japan*

²⁷*Institute of Astronomy, Graduate School of Science, The University of Tokyo, 2-21-1 Osawa, Mitaka, Tokyo 181-0015, Japan*

²⁸*Department of Physics, The Catholic University of America, Washington, DC 20064, USA*

²⁹*Institute of Space and Astronautical Science, Japan Aerospace Exploration Agency, 3-1-1 Yoshinodai, Chuo, Sagami-hara, Kanagawa 252-5210, Japan*

³⁰*Sorbonne Université, CNRS, UMR 7095, Institut d'Astrophysique de Paris, 98 bis bd Arago, 75014 Paris, France*

³¹*Department of Physics, University of Auckland, Private Bag 92019, Auckland, New Zealand*

³²*College of Science and Engineering, Kanto Gakuin University, 1-50-1 Mutsuurahigashi, Kanazawa-ku, Yokohama, Kanagawa 236-8501, Japan*

³³*University of Canterbury Mt. John Observatory, P.O. Box 56, Lake Tekapo 8770, New Zealand*

³⁴*Las Cumbres Observatory, 6740 Cortona Drive, Suite 102, Goleta, CA 93117, USA*

ABSTRACT

In the pursuit of understanding the population of stellar remnants within the Milky Way, we analyze the sample of ~ 950 microlensing events observed by the Spitzer Space Telescope between 2014 and 2019. In this study we focus on a sub-sample of nine microlensing events, selected based on their long timescales, small microlensing parallaxes and joint observations by the Gaia mission, to increase the probability that the chosen lenses are massive and the mass is measurable. Among the selected events we identify lensing black holes and neutron star candidates, with potential confirmation through forthcoming release of the Gaia time-series astrometry in 2026. Utilizing Bayesian analysis and Galactic models, along with the Gaia Data Release 3 proper motion data, four good candidates for dark remnants were identified: OGLE-2016-BLG-0293, OGLE-2018-BLG-0483, OGLE-2018-BLG-0662, and OGLE-2015-BLG-0149, with lens masses of $2.98^{+1.75}_{-1.28} M_{\odot}$, $4.65^{+3.12}_{-2.08} M_{\odot}$, $3.15^{+0.66}_{-0.64} M_{\odot}$ and $1.4^{+0.75}_{-0.55} M_{\odot}$, respectively. Notably, the first two candidates are expected to exhibit astrometric microlensing signals detectable by Gaia, offering the prospect of validating the lens masses. The methodologies developed in this work will be applied to the full Spitzer microlensing sample, populating and analyzing the time-scale (t_E) vs. parallax (π_E) diagram to derive constraints on the population of lenses in general and massive remnants in particular.

Keywords: Microlensing, Stellar remnants, Black Holes, Neutron Stars, Spitzer, Gaia

1. INTRODUCTION

Detecting and characterizing stellar remnants is vital for our understanding of the evolution of stars and populations in the Milky Way. Black holes, in particular, have been of great interest due to their role in the growth and formation of galaxies. Neutron stars offer unique insights into stellar evolution, extreme matter and fundamental physics. In addition, both can play a role in the distribution of dark matter in galaxies, which is still one of the biggest unresolved mysteries in astrophysics.

Detecting stellar remnants poses a challenging problem due to their typically dim and elusive nature. Historically, efforts to identify these remnants have relied heavily on indirect methods, that require the remnant to be in a binary system. For instance, the discovery of binary systems with compact objects, such as X-ray binaries, has provided crucial evidence of their existence. Notably, the detection of gravitational waves, pioneered

by the Laser Interferometer Gravitational-Wave Observatory (LIGO) and the Virgo collaboration (e.g. [Abbott et al. 2016](#)), marked a monumental advancement in the direct detection of stellar remnants, particularly black holes and neutron stars.

Still, single, non-accreting, stellar-mass black holes, as well as aged, isolated neutron stars, are practically inaccessible to date. Consequently, our knowledge about these celestial objects remains limited, although they hold valuable information related to stellar formation and evolution. The only practical way to observe them is through microlensing, i.e. by detecting their gravitational influence on the light from another object. Measuring the mass of the lensing object and constraining the flux that it emits allows us to assess if it could be a stellar remnant. The only known isolated, stellar-mass black hole was identified using this technique ([Sahu et al. 2022](#), [Lam et al. 2022](#), [Mróz et al. 2022](#), [Lam & Lu 2023](#)).

Microensing is inherently limited in terms of mass measurement due to its reliance on obtaining the Einstein radius θ_E from

$$M_L = \frac{\theta_E}{\kappa\pi_E}, \quad \pi_E = \frac{\pi_{\text{rel}}}{\theta_E}, \quad \pi_{\text{rel}} = \frac{1}{D_L} - \frac{1}{D_s} \quad (1)$$

where $\kappa = 8.144 \text{ mas}/M_\odot$, π_E is the magnitude of the microlensing parallax vector (see e.g. Gould 2004), D_L is the distance to the lens and D_s is distance to the source.

Direct measurements of θ_E are challenging to obtain in practice. In some cases it can be done through observations of caustic crossings, resolving the images using interferometry (Delplancke et al. 2001, Cassan & Ranc 2016) or astrometric microlensing (Dominik & Sahu 2000). All these approaches are somewhat sub-optimal for studying large populations of objects. The first requires very special circumstances to occur: a caustic-crossing of either a binary lens, or less likely, the central passage of a single lens in front of the source. The second, resolving the images with high-precision interferometers, is a promising avenue. Two such detections have been reported to date: for the Kojima event (Nucita et al. 2018), Fukui et al. 2019, Zang et al. 2020) and Gaia19bld (Cassan et al. 2022, Bachelet et al. 2022, Rybicki et al. 2022). Although this technique is limited to brighter targets, we should expect an increasing number of interferometric observations of microlensing events thanks to developments in the field (Gravity+ Collaboration et al. 2022, Gould 2023). The third approach to direct θ_E measurement is through astrometric microlensing, which requires a sub-milliarcsecond astrometric precision. This limitation will also slowly be overcome, especially thanks to the development of advanced space satellites like Gaia (e.g. Rybicki et al. 2018, Klüter et al. 2020) and Roman (e.g. Sajadian & Sahu 2023, Fardeen et al. 2024). It could also be possible to investigate seeing-limited data sets like OGLE or KMTNet (Segev et al. in prep.), where the number of measurements might help to overcome limited astrometric accuracy. However, up to now, success in observing astrometric microlensing has been limited. There are ongoing attempts to detect it using adaptive optics (e.g. Lu et al. 2016), but only limits were obtained from this kind of studies. The signal has been detected only in handful of events using the Hubble Space Telescope and under very special circumstances (Sahu et al. 2017, Zurlo et al. 2018, Sahu et al. 2022, McGill et al. 2023)¹. As of

today, it is still a technique that can only be applied to specific cases.

An alternative method for estimating the mass of the lens in microlensing events involves using the timescale of the event and microlensing parallax, while making assumptions about the distribution of proper motions, because $\theta_E = \mu_{\text{rel}}t_E$. Then, one would calculate the mass as

$$M_L = \frac{\mu_{\text{rel}}t_E}{\kappa\pi_E} = 1.35M_\odot \left[\frac{\mu_{\text{rel}}}{4 \text{ mas/yr}} \right] \left[\frac{t_E}{100 \text{ d}} \right] \left[\frac{0.1}{\pi_E} \right]. \quad (2)$$

However, this approach is reliant on assumptions about the proper motion distribution and galactic model, which can introduce uncertainties and biases in the final mass estimates. It is important to note, that with this approach one does not directly measure the mass of the lens, and only recovers statistical information about this parameter, depending on the assumed Galactic model. As mentioned before, it is also necessary to constrain the flux coming from the lens to be able to claim that it is a dark stellar remnant.

Several studies have already employed this mass estimation approach, where statistical information about μ_{rel} is applied. For example, Wyrzykowski et al. (2016) applied this method to the OGLE-III sample of 59 events exhibiting a parallax signal. Later, additional analysis was conducted for the same sample of events, but it also implemented the source proper motion from the Gaia Data Release 3 (GDR3) catalog, to tighten the prior on the relative proper motion distribution (Wyrzykowski & Mandel 2020). In the following studies, Mróz & Wyrzykowski (2021) refined and improved the technique, while Mroz et al. (2021) applied it again to the OGLE-III data set.

The crucial element of this approach hinges on the detection or, at the very least, constraint of the microlensing parallax signal within the selected sample's events. Unfortunately, the ground-based-only photometric measurements usually do not provide strong constraints on the microlensing parallax, as it requires the Earth accelerated motion around the Sun to be significant.

In addition, the more pronounced (and thus - easier to measure) the microlensing parallax signatures, the higher the value of the π_E parameter. This bias poses an even greater challenge in the examination of massive stellar remnants, as events with smaller microlensing parallaxes tend to favor more massive lenses (see Equation 1). One way to avoid such bias and also measure smaller π_E values, would be to rely on simultaneous space satellite observations to identify the microlensing parallax signal, instead of Earth's orbital motion.

¹ Gaia preliminary astrometric time series also confirmed the light centroid deviations in the Gaia16aye event https://www.cosmos.esa.int/web/gaia/iow_20210924

To utilize this idea, we reviewed the sample of ~ 950 events that have been a part of the Spitzer microlensing campaign, which was conducted in the 2014-2019 seasons. The Spitzer campaign was directed specifically towards the goal of extra-solar planet characterization. Nonetheless, the procedure of target selection and the observing strategy for the campaign is well defined (Yee et al. 2015), meaning it is a controlled sample, which allows drawing conclusions about the general stellar remnant population. In this study, we do not explore the whole population of stellar remnants based on the Spitzer sample, but rather select particular candidates with longer timescales and smaller values of the π_E parameter, which are likely to be caused by a more massive lens. Then, after assessing the amount of light that is emitted by the blend and the lens, one can judge whether the lens is a good candidate for a dark stellar remnant or not. Furthermore, we select and analyze only those events that were observed by the *Gaia* mission, as they might be verifiable in the near future, thanks to high precision astrometric measurements from *Gaia* that could be used to measure or constrain θ_E .

This paper is organized as follows. In Section 2.4 we present an initial review and analysis of the whole Spitzer microlensing sample, which is performed to populate an initial $t_E - \pi_E$ diagram, necessary to select candidates for stellar remnants lenses. In Section 3 we do an in-depth analysis of the nine events that were selected, including the derivation of lens mass and distance distributions, which utilizes our light curve analysis and priors on lens-source proper motions based on the Milky Way models. In Section 4 we simulate realistic *Gaia* astrometry for a range of possible θ_E values, including the most probable ones resulting from the analysis presented in Section 3. We summarize and give conclusions in Section 5.

2. POPULATING THE $t_E - \pi_E$ PLANE

To find the sub-sample of microlensing events hosting stellar remnants, we first need to populate the $t_E - \pi_E$ diagram, which will allow us to select potentially massive lenses. First, as we only consider standard (point source, point lens; hereafter PSPL) events with parallax, we filter out all the events with clear caustic-crossing or finite source signatures based on visual inspection. After this step, out of the ~ 950 Spitzer events, 720 remain. These events constitute our final sample that is used for the construction of the $t_E - \pi_E$ diagram.

2.1. Ground-based data

During the modeling procedure (see Section 2.3) we are fitting the PSPL model with parallax to the joint set

of OGLE+KMT+*Spitzer* data. In this step of unsupervised, automatic fitting we decide to omit MOA data for practical reasons, as OGLE+KMT sets are sufficient for creating an initial model. Later on, in a detailed analysis of individual events from the selected sub-sample, we use the full re-reduced data.

Triggering of targets in the Spitzer microlensing campaign was based on the OGLE EWS (Udalski et al. 1992, Udalski et al. 2015a) and MOA (Bond et al. 2001) alerts. The KMTNet (Kim et al. 2016) data were incorporated into the decision-making starting in 2016. The OGLE-IV data were collected with a large mosaic camera, consisting of 32 CCD chips with resolution 2048x4096 pixels each, and the scale of 0.26 arcsec/px. The camera is mounted on the 1.3-meter Warsaw Telescope, located in Las Campanas Observatory in Chile. The cadence for each event varied between $\sim 4/\text{hr}$ up to $\sim 0.5/\text{day}$, depending on the field, with the frequency of observations declining with the increasing (projected) distance from the Galactic center. The data were reduced with the OGLE-IV photometric pipeline (Udalski et al. 2015a), which implements an improved DIA procedure from Wozniak (2000). Full OGLE-IV light curves were used, with the data collected up until² $HJD' \approx 8920^3$.

The KMTNet survey uses three 1.6-meter telescopes, located in Cerro Tololo Inter-American Observatory (CTIO, Chile), Siding Spring Observatory (SSO, Australia) and South African Astronomical Observatory (SAAO, South Africa). Each telescope has a mosaic camera with 4, 9k x 9k CCD chips mounted and a pixel scale of 0.4 arcsec/px. As the majority of events have good OGLE coverage, in this initial step of building an initial $t_E - \pi_E$ diagram it is sufficient to use publicly available KMTNet data from the automatic pipeline, which is only the part of the light curve from the discovery season for each event. In the detailed analysis of smaller sub-sample we use all the available, re-reduced data.

2.2. Spitzer data

The Spitzer Space Telescope microlensing campaign was conducted during the “warm” part of the mission and so the data were collected using the IR, narrow bandwidth L , centered at the wavelength of 3.6 μm . While covering the peak of the event is the most beneficial for the microlensing parallax determination, the

² Which marks the beginning of the 2020 bulge season and is a practical cut-off date for observations of 2019 (and earlier) events, given that OGLE paused its operations because of the COVID-19 outbreak at this time.

³ $HJD' \equiv HJD - 2450000$

satellite observations usually only cover a part of the light curve, as there is a delay between the target selection and the actual observation time. Naturally, it is also not known *a priori* when exactly the event is going to peak from the Spitzer perspective.

Each year, targets could have been observed by Spitzer during either of the two, ~ 38 day long windows (Northern summer and winter), when the Galactic bulge was visible from the satellite’s location (Calchi Novati et al. 2015). In practice, most of the events were only observed within the summer window, as during the winter the Galactic center is not accessible for Earth-based instruments. There were a few exceptions, where the event was either observed in multiple years (mostly for the baseline information), or during the winter window. In fact, a few events from the selected “massive” sub-sample did get such additional winter observations, which significantly enhanced the microlensing parallax measurements (see Section 3). Nonetheless, in the full, 950-event sample of Spitzer microlensing events, most of the targets have only one patch of Spitzer data, taken within the summer window, with ~ 1 day cadence, over a period of $\sim 2 - 5$ weeks.

The rough description and numbers quoted above, while not detailing exact information for every specific event, provide the needed understanding of the Spitzer light curves’ coverage that is sufficient for the goals of our work. The specific details of the Spitzer microlensing campaign, its observing strategy, target selection criteria are beyond the scope of this paper. More information can be found in e.g. Yee et al. (2015) and Udalski et al. (2015b). The detailed analysis of the whole Spitzer microlensing sample, which will be used for more general studies of the population of the Galactic planets and stellar remnants, will be presented in a separate paper.

2.3. Light curve modeling

To construct the initial $t_E - \pi_E$ plane and identify the events with potentially massive lenses, we fit a standard PSPL microlensing model with parallax to the 720 events that were not classified as “clearly binary” during the initial, visual inspection. In our light curve analysis we use procedures from the `pyLIMA` package (Bachelet et al. 2017) which employs `VBinaryLensing` code for light curve computation (Bozza et al. 2018).

First, we re-scale error bars in all the data sets, which is necessary to obtain meaningful parameter uncertainties and to compare different models. We apply the re-scaling procedure in steps to consecutive groups of data sets, fixing the error bars in the groups that have already been modified. We start with fitting to the OGLE data as it has the most stable photometry and long baseline.

We first fit a PSPL model, which is then used as a seed for the two ($u_0 > 0$ and $u_0 < 0$) fits of PSPL+parallax models. Out of the these two fits we pick the one with the better χ^2 to be a reference. We then apply a standard formula for the new error bars (e.g. Yee et al. 2012):

$$\sigma_{\text{new}} = \sqrt{(\gamma\sigma_{\text{old}})^2 + \epsilon^2}, \quad (3)$$

where we fix the value of the error floor $\epsilon = 0.005$ mag for all data sets but *Spitzer*, for which we do not set the floor for the error. We find the re-scaling factor γ by requiring $\chi^2/dof = 1$. This procedure is repeated multiple times, which iteratively removes outliers. After the whole procedure is finished for the OGLE data, we add all the other ground-based sets, and finally, the *Spitzer* data.

Starting with a simple least-squares minimization, we fit a PSPL model to the re-scaled ground-based data. We calculate the model using the standard formula for the magnification (e.g. Paczynski 1986):

$$A(u) = \frac{u^2 + 2}{u\sqrt{u^2 + 4}}; \quad u(t) = \sqrt{u_0^2 + \left(\frac{t - t_0}{t_E}\right)^2}, \quad (4)$$

where t_0 , u_0 and t_E are the standard microlensing parameters: time of maximum, smallest projected separation in the units of Einstein radius and Einstein timescale, respectively. The magnification enters the formula for total flux that is changing during the event:

$$F_{\text{tot}}(t) = A(t)F_s + F_{\text{bl}}, \quad (5)$$

where F_s is the flux from the source and F_{bl} is flux from the blend. During the modeling procedure we include the blend flux through the blending parameter

$$g = \frac{F_{\text{bl}}}{F_s}. \quad (6)$$

We use the derived Paczyński parameters (t_0 , u_0 , t_E) as a seed in the next fitting step. Then, before the final step, we fit a model with parallax to the ground-based data only, to assess the microlensing parallax signal resulting from Earth’s orbital motion. The model incorporates two additional parameters: North and East components of the microlensing parallax vector $\boldsymbol{\pi}_E = (\pi_{\text{EN}}, \pi_{\text{EE}})$ (see e.g. Gould 2004 for details). Finally, the joint fit to all space and ground-based data is performed, where both annual, and space parallax effects have to be taken into account.

The space parallax also allows constraints on the $(\pi_{\text{EN}}, \pi_{\text{EE}})$ vector. Having a satellite at projected distance D_\perp from Earth, allows calculation of the microlensing parallax based on the difference between the

t_0 and u_0 parameters measured from the ground and from space (e.g. Refsdal 1966, Gould 1994):

$$\pi_{\mathbf{E}} = \frac{\text{au}}{D_{\perp}}(\Delta\tau, \Delta u_0), \quad (7)$$

where

$$\Delta\tau = \frac{t_{0,\text{sat}} - t_0}{t_{\mathbf{E}}}, \quad \Delta u_0 = u_{0,\text{sat}} - u_0, \quad (8)$$

and the *sat* subscript refers to parameters measured from the perspective of the satellite. The space-based measurement of the microlensing parallax is independent from the ground-based measurement, which allows for an additional cross-check between the two.

In both ground-based-only and full parallax fitting we explore $u_0 > 0$ and $u_0 < 0$ regimes separately, which usually results in two, similarly well fitted models. While in principle we do expect up to four solutions (the so called four-fold degeneracy, see e.g. Gould 2004), at this stage of analysis we limit ourselves only to search for the $u_0+ \leftrightarrow u_0-$ degeneracy. Because during the fitting procedure we start from $\pi_{\mathbf{E}} = (0, 0)$, we expect the solution to converge to the smaller values first, and thus we might not be finding solutions with large $\pi_{\mathbf{E}}$ values. While for complete analysis of each event the full grid search has to be done, we accept this limitation in this work, as our goal is to find potentially massive lenses, i.e. those with smaller parallaxes. Then, for the selected nine candidates we explore the full $\pi_{\text{EN}} - \pi_{\text{EE}}$ space (see Section 3 for detailed analysis and selection criteria).

2.4. Initial $t_{\mathbf{E}} - \pi_{\mathbf{E}}$ plane

Having PSPL models with parallax fitted to all the non-binary light curves from the Spitzer sample of microlensing events, we were able to build an initial $t_{\mathbf{E}} - \pi_{\mathbf{E}}$ plane (Figure 1). All the events have two solutions, as for each event the u_0- and u_0+ planes were separately explored (see Section 2.3). As in further analysis we are specifically interested in massive lens candidates, in Figure 1 we are plotting the solution that results in a higher expected mass of the lens (see Equation 1). We mark the events that were observed by the Gaia mission (blue crosses and green circles). From among them we choose the ones that host potentially massive lens (red diamonds) - those are analyzed in detailed as good candidates for dark remnants (see Section 3).

The majority of the events lie approximately in the middle of the presented space, but one might identify two distinct, smaller groups: one with large microlensing parallax values, clumped at $\pi_{\mathbf{E}} \approx 2$ and one with long timescales of $t_{\mathbf{E}} \approx 500$ days, which is the internal, upper limit on this parameter value in the fitting algorithm. Events in both groups (in total ≈ 40) suffer from

faulty fits. After visual inspection of the light curves and fitting results, we conclude that the reason is either low SNR of ground-based data, significant systematic trends (likely due to proper motion of the source/lens, which impacts DIA reduction procedure), or a low number of Spitzer data points. All of these factors, and particularly their combination, lead to inaccurate microlensing parallax measurements, especially if the effect is small. As a result, the fitting algorithm converges to parameter values that are inaccurate or wrong, or does not converge at all. While most of these issues can be addressed either by careful re-modeling, de-trending or simply filtering-out impacted light curves, such analysis is beyond the scope of this paper. There are no events observed by *Gaia* in these groups and so they would not enter the final sample, although we still plot them here for the sake of completeness.

3. MASSIVE LENS CANDIDATES

In this section we describe the analysis of the sub-sample consisting of candidates for potentially massive lenses.

3.1. Sample selection

There were three general criteria used during the selection procedure: long Einstein timescale $t_{\mathbf{E}}$, low value of microlensing parallax $\pi_{\mathbf{E}}$ and presence of Gaia data. The first two together makes higher values of lens mass $M_{\mathbf{L}}$ more likely, although we note that it also depends on the lens-source relative proper motion (Equation 1). The last condition makes the mass of the lens (potentially) verifiable in the near future, thanks to the Gaia astrometry - see Section 4 for the analysis of this aspect. Construction of the initial $t_{\mathbf{E}} - \pi_{\mathbf{E}}$ diagram for all the PSPL Spitzer events allows easy selection of candidates according to the criteria described above. We refrain from applying strict cuts on the parameters, as there is no clear reason for such. Our sub-sample will not be representative for the stellar remnant population and the selection procedure will be arbitrary anyway. We pick mostly events lying below the gray, dashed line on figure 1, i.e. those for which the more massive solution results in $M_{\mathbf{L}} > 1.4 M_{\odot}$ (as a lower limit on the mass of neutron stars), under the assumption of $\mu_{\text{rel}} = 4$ mas/yr. We supplement this sample with event OGLE-2015-BLG-0145, which, although it lies above the gray line, has a long timescale of $t_{\mathbf{E}} \gtrsim 100$ days and with its relatively small $\pi_{\mathbf{E}}$ value might still be considered as a good candidate.

This results in a sub-sample of 9 candidates (red diamonds on Figure 1) for stellar remnant lenses, for which we perform a more detailed analysis. With the addi-

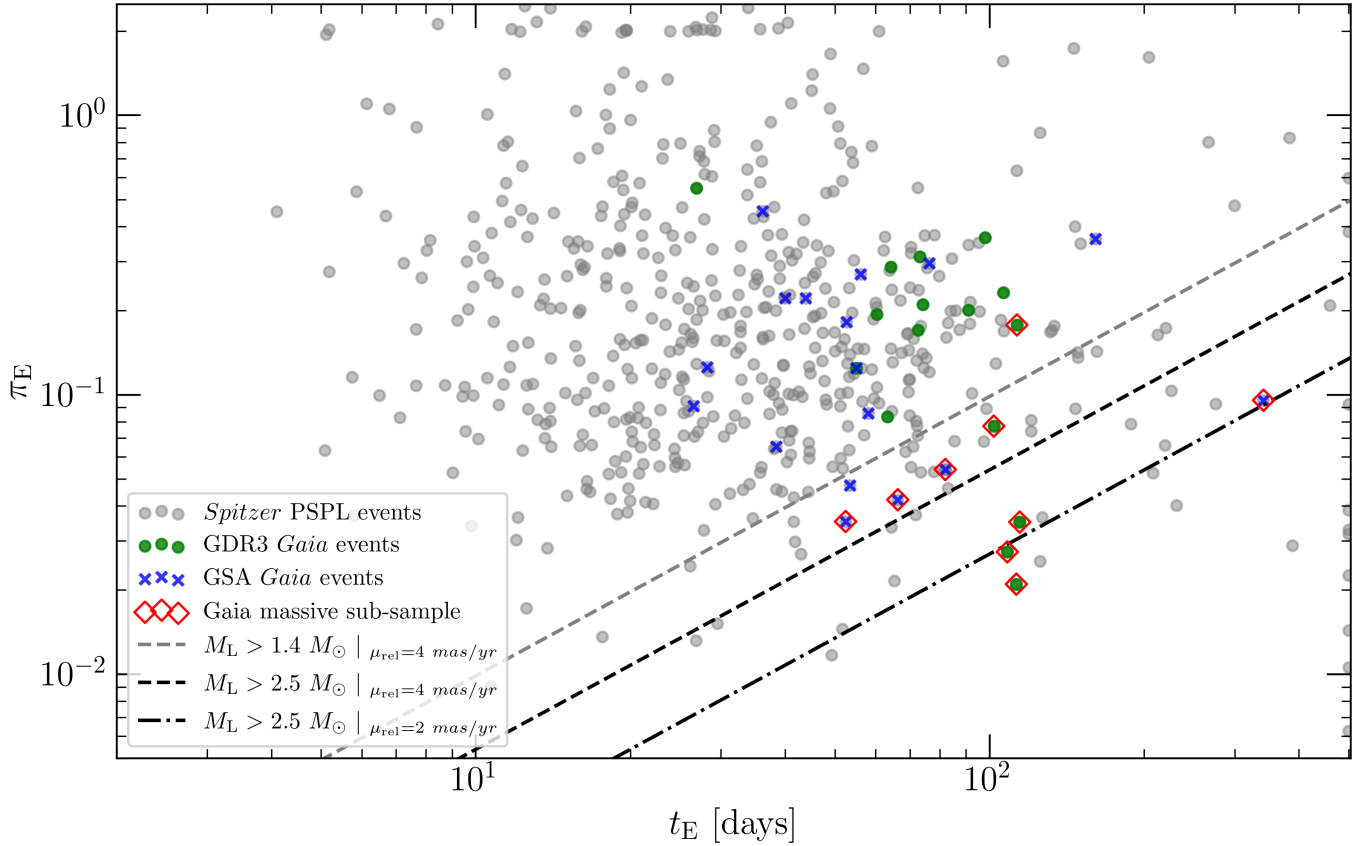


Figure 1. Initial $t_E - \pi_E$ plane, populated with the results from parallax PSPL fit to all Spitzer events (gray points). Colored crosses and circles mark all the events that were also observed by Gaia mission and published either through Gaia Science Alerts (blue) or in Wyrzykowski et al. 2023 (green). Red diamonds mark those events that were selected for detailed analysis as they host potentially massive lenses. For a given value of relative lens-source proper motion, one can draw a line of constant lens mass. Assuming a typical value of $\mu_{\text{rel}} = 4$ mas/yr, all the events lying below the gray line would be caused by lenses heavier than $1.4 M_\odot$, while those below the black line are caused by lenses heavier than $2.5 M_\odot$. To visualize the impact of proper motion, we also plot the dash-dotted line for $\mu_{\text{rel}} = 2$ mas/yr and $M_L = 2.5 M_\odot$. We note that there are two groups of events with faulty fits: one with high values of t_E (~ 5000 d) and the other with π_E (~ 2) - see Section 2.4 for details.

tional source color analysis described below, we can measure the parallax signal more accurately, which in turn leads to more reliable predictions of the physical parameters of the lens, presented in Section 3.7.

3.2. Gaia photometric data

Currently there are two groups of microlensing events observed by *Gaia* that have photometric time-series publicly available. The first group consists of all events published through Gaia Science Alerts (Hodgkin et al. 2013, 2021, henceforth GSA). Once an alert is announced through this channel, all the *Gaia* photometry for the target is published. The second group is the *Gaia* DR3 microlensing catalog (Wyrzykowski et al. 2023). Because it was constructed using DR3 data, it only contains measurements collected up to \sim May 2017. In the last column of Table 3 we mark which events from our sample were alerted by GSA, and thus have a full *Gaia* light curve available.

Most of the photometric observations from the *Gaia* satellite are taken in *G*-band, and only these are used in this work during the construction of the light curve model. The photometric measurements for the events detected through GSA do not have uncertainties reported, and so we estimate them based on the *Gaia* DR2 photometric content and validation paper (Evans et al. 2018).

On average, *Gaia* comes back to the same field every ~ 30 days, and every visit it takes two measurements separated by ~ 6 hours (each for one of the mirrors), although this number can vary depending on the gradient of the scanning angle (Gaia Collaboration et al. 2016). Although such frequency of observations is insufficient to properly cover a microlensing light curve, *Gaia* photometry is only playing a supplementary role in the process of light curve characterization. In particular, we do not detect any meaningful signal of space

Table 1. Re-scaling factors γ for each telescope, along with the number of photometric data points used.

Event ^a	Telescope	γ	N points
OB150145	OGLE	1.4	554
	Spitzer	1.6	48
	Gaia	1.7	31
OB150149	OGLE	1.4	1653
	Spitzer	4.5	50
	Gaia	5.0	41
OB150211	OGLE	1.2	937
	Spitzer	4.7	109
	Gaia	1.5	28
OB160293	OGLE	1.6	2718
	Spitzer	3.1	24
	Gaia	1.9	32
	KMTS	1.0	1404
	MOA	2.2	1798
OB160689	OGLE	1.4	1162
	Spitzer	2.7	16
	Gaia	1.7	21
	KMTA	1.1	442
	KMTC	1.0	726
	KMTS	1.1	662
OB180410	OGLE	1.7	2660
	Spitzer	1.9	29
	Gaia	1.1	80
	KMTA	3.1	190
	KMTC	1.6	369
	KMTS	1.9	179
OB180483	OGLE	1.4	1170
	Spitzer	1.9	27
	Gaia	0.6	39
OB180662	OGLE	2.3	952
	Spitzer	2.4	44
	Gaia	0.5	59
	KMTA	1.4	395
	KMTC	1.1	821
	KMTS	1.3	359
OB190169	OGLE	5.0	955
	Spitzer	2.5	33
	Gaia	1.6	52
	KMTS	2.1	3610

^a For simplicity, a shortened version of the event names are used in tables and figures throughout the paper: OBXXYYYY \equiv OGLE-20XX-BLG-YYYY.

parallax in the *Gaia* data (which is expected as *Gaia* is in orbit around Lagrange point L_2 , much closer to the Earth than the *Spitzer* satellite). On the other hand, the astrometric data it will provide, not only will be crucial for the light centroid shift detection (see Section 4), but also do not require as high cadence as photometry to be useful, due to much longer effective time scale of the astrometric microlensing signal compared to its photometric counterpart (e.g. Dominik & Sahu 2000).

3.3. Additional ground-based data

In the analysis of the OGLE-2016-BLG-0293 event we also included data from MOA collaboration (Bond et al. 2001). The photometric measurements were taken with the 1.8 m telescope located at Mt. John, New Zealand, using their standard broad R filter.

To determine the color of the source (see Section 3.5) for the OGLE-2015-BLG-0211 event, we used the H -band measurements from the *ANDICAM* instrument (DePoy et al. 2003), mounted on the 1.3m SMARTS telescope located in the CTIO observatory in Chile.

3.4. Source stars

Generally the information about the color of the source and the position of the source and the blend on the CMD is useful to investigate potential inconsistencies in the model. It is also necessary to support the space parallax calculations based on the *Spitzer* data (see the next sub-section). To perform a source color analysis, observations of the event in a second band are required. Having regular coverage in two bands that span a reasonably large range of magnifications throughout the event, we are able to derive the source color independently of the model. Linear regression is used to fit the relationship between the total fluxes in both bands, as the slope of the linear function is equivalent to the source flux ratio in the two bands, which directly translates to the source color (see Equation 5). Whenever it is possible, the color analysis is made based on the OGLE data set as it is the one with longest baseline and most reliable photometry. Excluding OGLE-2015-BLG-0211 all the events in our sample have the OGLE V -band available and so the $(V - I)_{OGLE}$ color of the source is derived. Most of the sources reside in the red clump (see Figure 2), which suggests that they are red giants that belong to the galactic bulge population. For the case of OGLE-2015-BLG-0211 we use the follow-up data in H -band to construct the CMD diagram and conclude that source is also part of the red clump.

3.5. *Spitzer* color constraints

The *Spitzer* data often do not allow measurements of the L -band baseline flux, which makes the π_E analysis

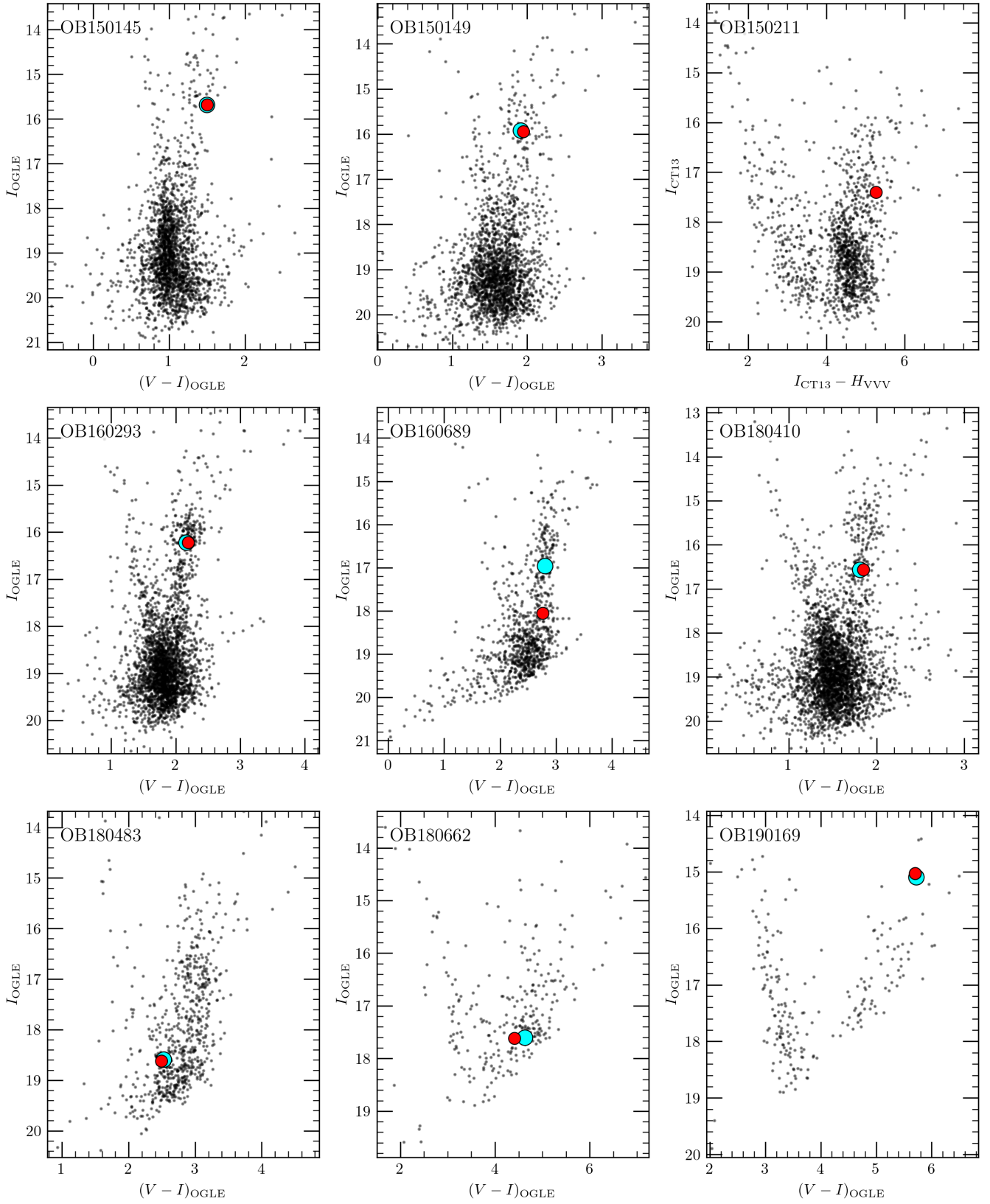


Figure 2. Color-magnitude diagrams for all the massive-lens candidate events, constructed from the indicated catalog of stars (mostly OGLE, in all events but OGLE-2015-BLG-0211) in a $2' \times 2'$ box around the magnified object. The large, red dots mark positions of the source stars while the cyan one mark the color and brightness of the baseline (i.e. including blend). They overlap whenever the blending is low, which is the case for almost all events in the sub-sample, excluding OGLE-2016-BLG-0689.

less constrained. It is possible to enhance the microlensing parallax information inferred from *Spitzer* observations by finding the color of the source $(I - L)_{\text{src}}$ and using it as a constraint on the *Spitzer* source brightness L during the modeling process⁴. To do that, we match stars detected in both OGLE and *Spitzer* frames and construct a color-color diagram, using I , V and L bands (so called *VIL* relation, see Calchi Novati et al. 2015 for details). For this purpose we use stars from the red clump, and so we expect such color-color relation to be linear for most of the sources. Using linear regression, we can find its functional form and, by interpolating (or extrapolating) to the known values of the source color $(V - I)_{\text{src}}$, derive $(I - L)_{\text{src}}$.

Such a constraint is expected to have the highest impact on the light curve fitting for the cases where *Spitzer* data only constrain the local slope of the light curve (which is often the case). We perform the modeling with and without the constraint and note significant improvement introduced by the color constraint for almost all events. The exception is the case of OGLE-2018-BLG-0662, where *Spitzer* covered part of the peak, already constraining the shape of the light curve sufficiently.

3.6. Light curves and modeling

To make sure there are no other solutions due to the four-fold degeneracy (Gould 2004), and to correctly probe the $(\pi_{\text{EN}}, \pi_{\text{EE}})$ space, we perform a dense grid search over these two parameters. We do the search separately for three fits: ground-based-only, *Spitzer*-“only” (Gould et al. 2020) and joint (using all data sets). The *Spitzer*-“only” approach is fitting the model to the ground-based data first and then, after fixing t_0 , u_0 and t_E , fitting $(\pi_{\text{EN}}, \pi_{\text{EE}})$ and source/blend fluxes using only *Spitzer* data. Although the accuracy of this approach can be limited, as it does not involve simultaneous fitting of all the parameters, it is useful to gain a better insight into the constraints on the parallax introduced by the ground and space-based data. In theory, given constraint on the source flux, each *Spitzer* measurement provides a circular constraint on the $(\pi_{\text{EN}}, \pi_{\text{EE}})$ plane (Gould 2019). In practice, the data are taken in different epochs and have a non-zero dispersion. As a consequence, the *Spitzer*-“only” parallax contours for real events form elongated arcs, which might be reduced further and provide constraints in both dimensions, for the cases where the *Spitzer* measurements cover larger parts of the light curve or are closer to the peak.

In the Figures 3 and 4 we gathered relevant parts of the parallax contours for all three modeling approaches.

⁴ L denotes *Spitzer*’s $3.6\mu\text{m}$ band.

Light curves for the most preferred solutions and a table with the fit parameters are presented in Figure 5 and Table 2, respectively. We present a more detailed discussion and comment on the analysis of each event separately in the following sub-sections.

OGLE-2015-BLG-0145

The u_0+ solution shows nonphysical negative blending level with $g_{\text{OGLE}} = -0.7 \pm 0.12$. The u_0- solution also yields negative blending, but consistent with zero at $g_{\text{OGLE}} = -0.06 \pm 0.12$. The u_0- model is also preferred in terms of the goodness of fit⁵, as $\Delta\chi^2 \approx 18$. In addition, the *Spitzer*-“only” parallax measurement is slightly more compatible with the ground-based-only measurement for the u_0- case, although for the u_0+ solution the two fits also remain in reasonably good agreement.

OGLE-2015-BLG-0149

While OGLE covered the full event, KMT only observed this event starting in 2016, so there is only the tail of the declining part of the light curve available from this survey. The event lasts for ~ 100 days and *Spitzer* measured only a part of the (rising) slope so most of the parallax information comes from the ground-based light curve, even after including the *VIL* color constraint. As one can see from panels *C* and *D* of Figure 3, *Spitzer*-“only” and ground contours are consistent. Blending behaves well and is consistent with zero for both u_0+ and u_0- solutions. The u_0- is somewhat preferred according to the photometric models, with $\Delta\chi^2 \approx 19$.

OGLE-2015-BLG-0211

The event lies in a highly extinguished field and so there are no measurements in the V_{OGLE} band that could be used to estimate the source color (from GDR3 we can have a very rough estimate of the $V - I$ color as $BP - RP = 4.52$ mag). Instead, we used additional observations in H -band. The data points were distributed over a large part of the light curve, which allowed for the source color determination.

Spitzer data with a color constraint allows refinement of the microlensing parallax constraints obtained based on the ground-based data (panels *E* and *F* in Figure 3). Both u_0+ and u_0- solutions have similar χ^2 ($\Delta\chi^2 \approx 2$) and so one can not assess which one is preferred based only on the photometric data.

OGLE-2016-BLG-0293

⁵ The photometry error bars are re-normalized, and so $\chi^2/dof \approx 1$ for all the events (see Table 2). Thus, when comparing different models, we use $\Delta\chi^2$ without quoting the number of *dof* throughout the text.

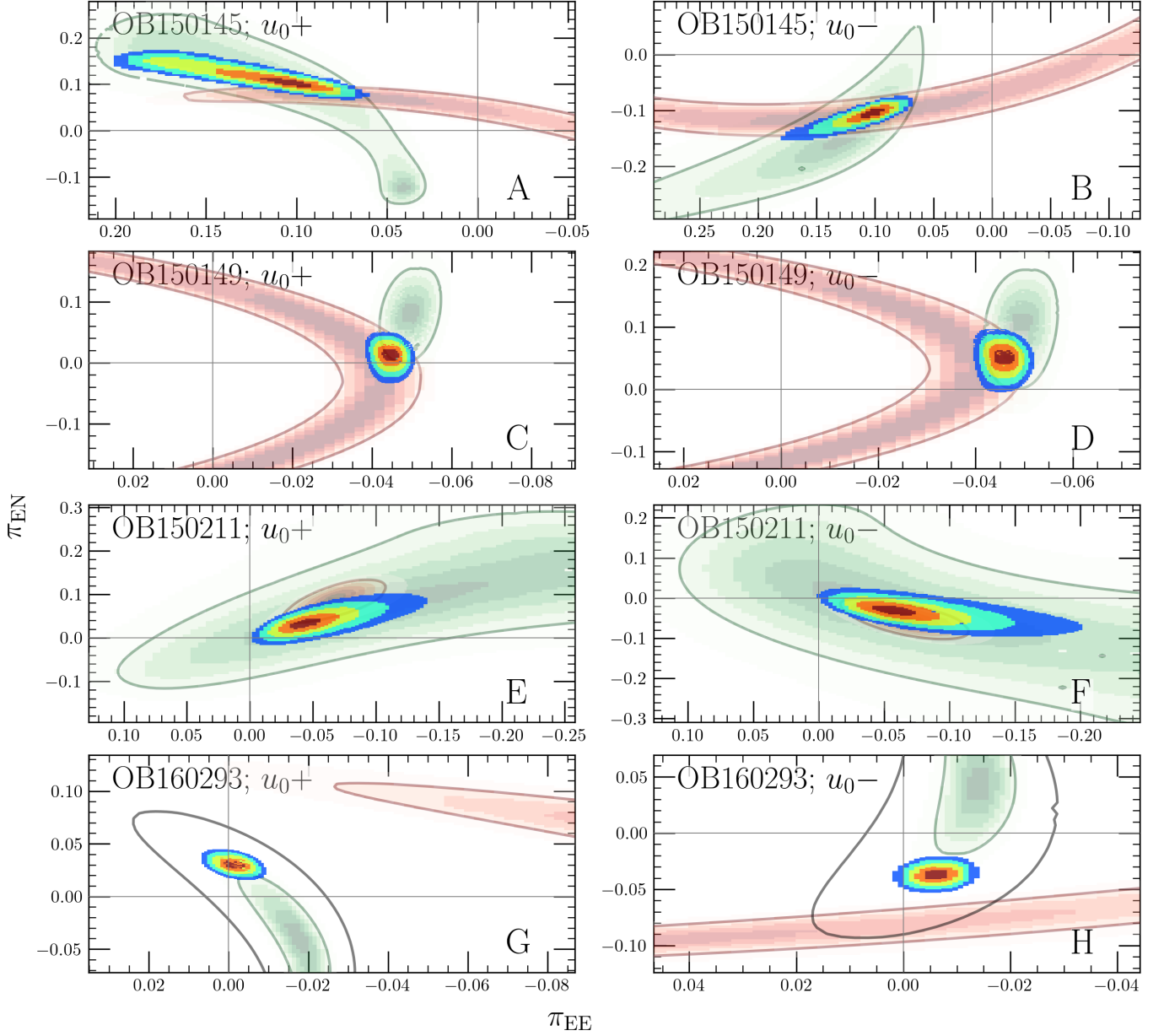


Figure 3. Microlensing parallax contours for u_0+ and u_0- solutions for the first four events in the selected sub-sample. Green and red outlines represent the 5- σ level for ground-based and Spitzer-“only” (with color constraint) fits, respectively. The colored, filled contours changing from dark red to blue represent 1-5 σ levels of the final, joint fit. For the events where additional ground-based data sets beyond OGLE were used, we also provide ground parallax contour based only on the OGLE data (gray), to track potential systematics.

In the OGLE-*I* and MOA data, short- and long time-scale systematics are visible. That being said, the source is relatively bright, and so some level of baseline variability is expected. In the OGLE data it is comparable to the scatter, and does not seem to have a large impact on the overall fit quality, but in the MOA data, the long time-scale baseline systematics are much more prominent. We address that issue by checking for any color changes in the OGLE *I*-band and *V*-band data, and potential correlations between the baseline color

and magnitude changes, which would imply astrophysical origin. The additional analysis do not show such color changes or correlations. Also, trends visible in the MOA data are not compatible with the smaller trends in the OGLE data, and so we conclude that larger systematics visible in MOA should not be taken into account. Thus, we discard the part of the MOA data affected the most and only include the measurements collected at $HJD' > 7000$.

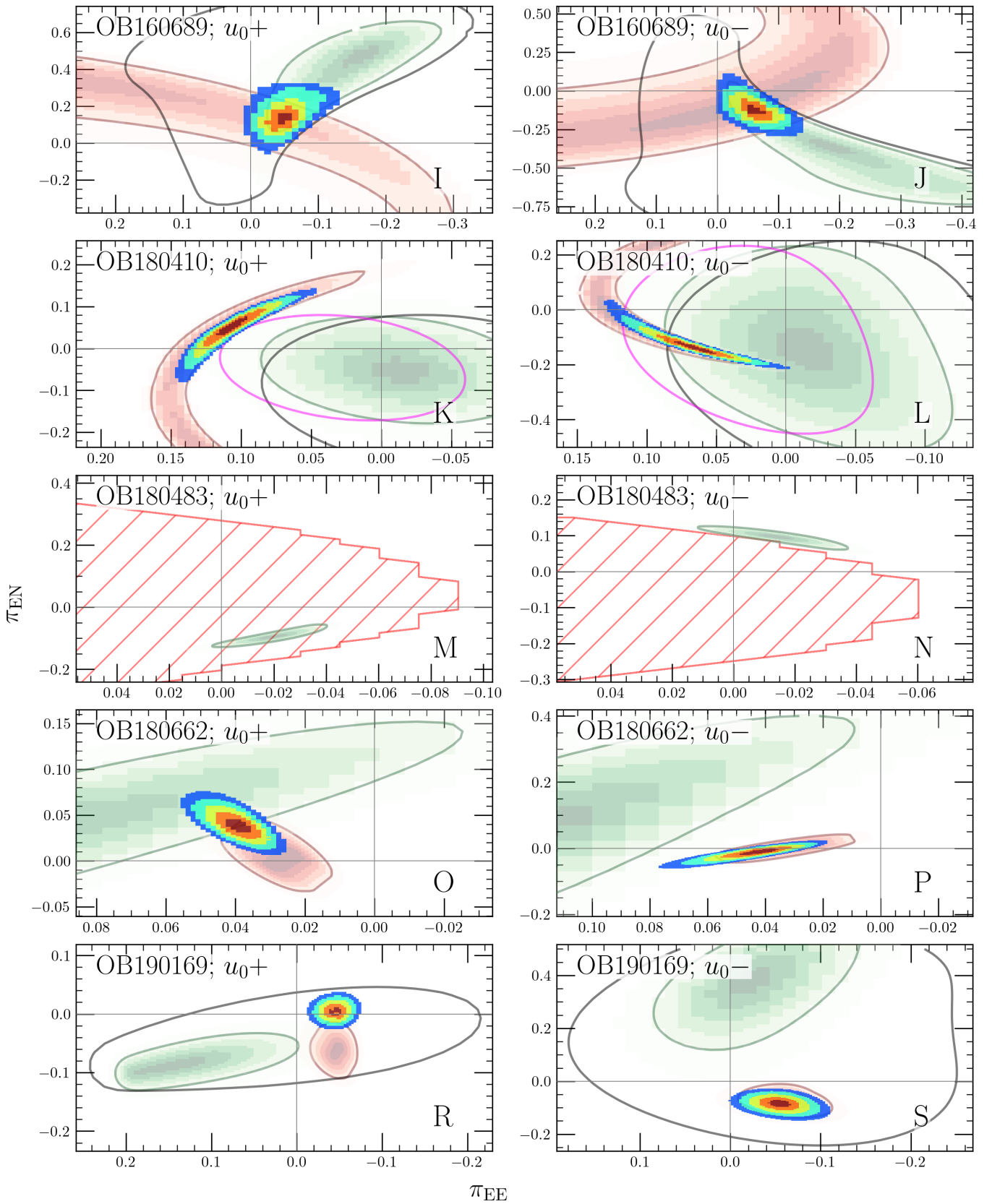


Figure 4. Same as Figure 3, for the remaining 5 events. For the case of OGLE-2018-BLG-0483 the *Spitzer* data allowed only for estimation of the upper limit on the flux, which excludes part of the $\pi_{EN} - \pi_{EE}$ space (marked with red, hatched area on panels M and N). The magenta contours on panels K and L represent ground-based-only fits with fixed blending parameter $g = 0$.

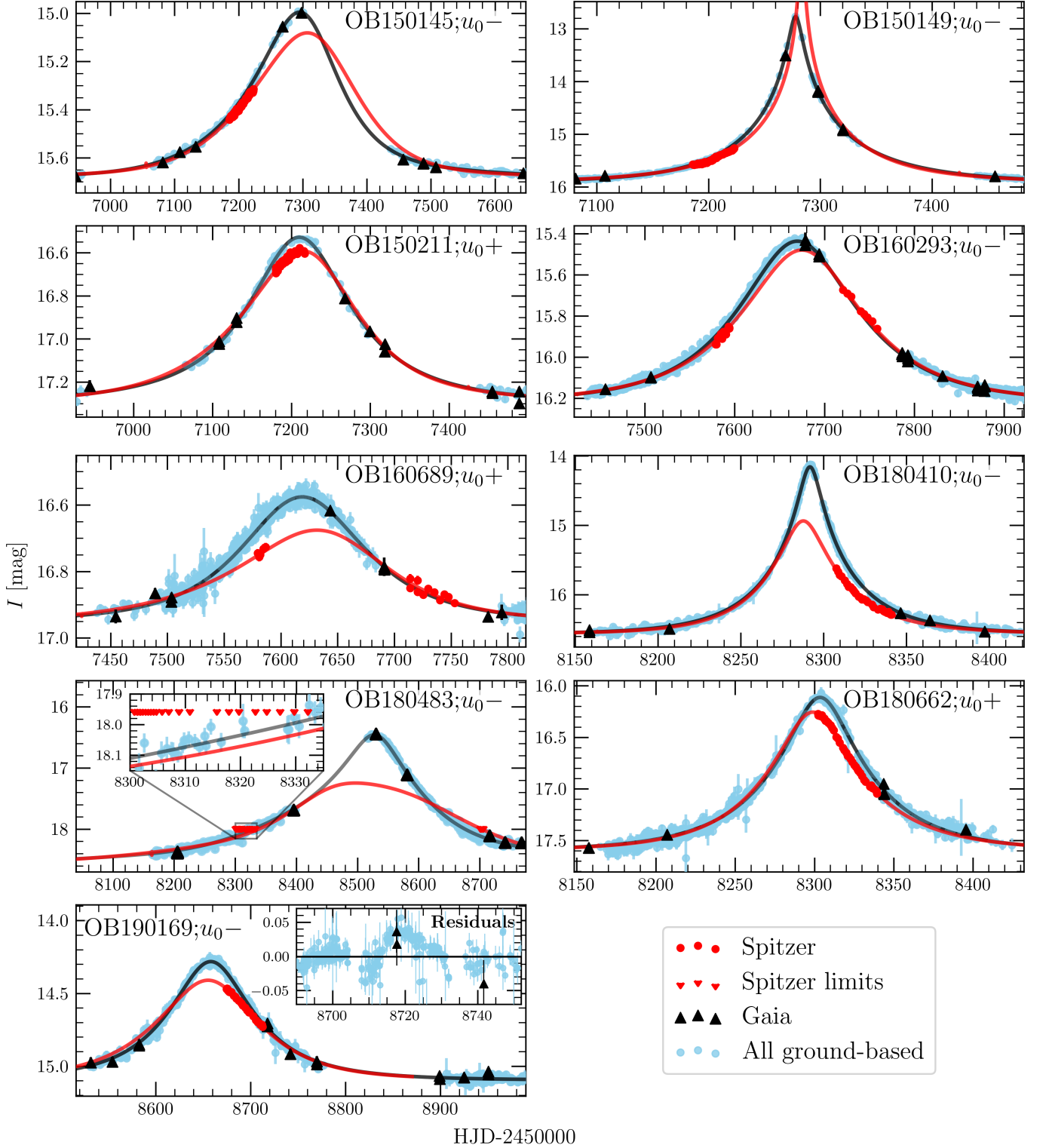


Figure 5. Light curves of all the events from our Spitzer-Gaia sub-sample, with all the data sets used during the modeling. Solid lines represent the best fit of PSPL+parallax model, showing Earth/Gaia (black line) and Spitzer (red line) perspectives. The ground-based data from all the surveys are plotted together (blue points). All models and data points are displayed with respect to I_{OGLE} baseline brightness. For the case of OGLE-2018-BLG-0483 we only derive limits on the *Spitzer* flux which is represented by downward triangles. Inset on the bottom left panel shows residuals of the region with a small deviation that might have been caused by a low-mass companion to the lens (see details in the text).

For the case of OGLE-2016-BLG-0293 we are able to discriminate between the two solutions, as there are multiple lines of evidence against the u_0+ one. First of all, there is a small difference $\Delta\chi^2 \approx 6$, which favors the negative solution. In addition, there is an evident disagreement between the ground-based-only and *Spitzer*-“only” parallax fits for the u_0+ case. Finally, the blending value obtained in the u_0+ solution is negative, and not consistent with zero ($4\text{-}\sigma$ away, see Table 2).

Including additional photometry beyond OGLE data set causes increasing inconsistency between the *Spitzer*-“only” parallax contours and the ground-based-only contours (see panel *H* of Figure 3). However, as we mentioned before, the *Spitzer*-“only” fit is only a diagnostic tool, and a general agreement between the two contours is sufficient to claim that the two sources of the microlensing parallax measurement are consistent for the u_0- case.

OGLE-2016-BLG-0689

For this event, in addition to the “regular” *Spitzer* observations, the data were also taken in the December window, which resulted in covering both the rising and declining part of the light curve. Thanks to that it was possible to determine the microlensing parallax relatively well.

While the blending for both of the solutions is consistent with zero, the posterior distribution for this parameter is also very wide, meaning that the blending parameter is not well constrained from the light curve. Indeed, the blending seems to be present as the source color and baseline color are different (see Figure 2). Additionally, there are only 2 points in the OGLE *V*-band on the magnified part of the light curve, which makes the source color determination more uncertain. Thus, we treat the *Spitzer* source color constraint with caution and conservatively use a wider prior on the *Spitzer* source color during the fitting ($3\text{-}\sigma$ instead of $1\text{-}\sigma$ resulting from the linear regression procedure described in Section 3.5). The u_0+ and u_0- solutions are similar in terms of the goodness of fit ($\Delta\chi^2 \approx 4$). The u_0+ has significant negative blending, but consistent with zero at $g_{OGLE} = -0.31 \pm 0.21$.

OGLE-2018-BLG-0410

After investigation of the photometric data we noted that MOA data shows large deviations that are not present in the remaining two surveys (especially at the wings of the event), and so we decide not to use it in the analysis. *Spitzer* data only cover part of the decline of the light curve and by itself provide rather sparse limits

on the microlensing parallax measurements. Nonetheless, performing *Spitzer*-“only” analysis and including the *VIL* color constraint, shows that space-based parallax gives two, relatively well defined χ^2 minima in $\pi_{EN} - \pi_{EE}$ space for each of the u_0+ and u_0- solutions. The u_0- is preferred with $\Delta\chi^2 \approx 19$, and is also much more convincing in terms of consistency between the *Spitzer*-“only” and ground-based-only parallax measurement, which can be seen from panels *K* and *L*, Figure 4. In addition, the blending is negative in both ground-based-only solutions, and not consistent with zero ($3\text{-}4\sigma$ away). To address this problem we decide to redo the fitting procedure with blending fixed to zero. Although the fit is clearly worse in terms of goodness (with the χ^2 difference of 8 and 20, see Table 2), the tension between the ground-based-only and *Spitzer*-“only” parallax disappears, at least for the u_0- solution (see magenta contours on panels *K* and *L*).

OGLE-2018-BLG-0483

The event was observed by *Spitzer* in two seasons, separated by about a year, but *Spitzer* gives no significant constraints on the parallax. Due to the low signal to noise ratio and crowding of the sky region around the event, we were only able to set limits on the *Spitzer* flux (see the zoom-in in Figure 5). As a result, it was only possible to exclude part of the central region in the $\pi_{EN} - \pi_{EE}$ space (see Figure 4, panels *M* and *N*). Still, the microlensing parallax can be accurately determined from the ground, which is not surprising as the event is extremely long - Einstein timescale is either ~ 275 or ~ 330 days, depending on the solution. The u_0+ solution has negative blending only marginally consistent with zero ($g_{OGLE} = -0.15 \pm 0.05$), which might suggest that the u_0- solution is the real one. More importantly, the u_0+ seems to be excluded by the *Spitzer* limits (Figure 4, panels *M* and *N*).

OGLE-2018-BLG-0662

Before fitting the final light curve model, the OGLE data were corrected for a small linear trend (≈ 0.04 mag over 10 years), likely caused by the change of the source position compared to the position on the reference image. The correction had a minor effect on the final results of the fit.

The microlensing parallax for the OGLE-2018-BLG-0662 event is weakly constrained from the ground, but with the addition of *Spitzer* data, a high precision π_E measurement was achieved, as the satellite covered part of the peak. In both the u_0+ and u_0- solutions, the blending is consistent with zero with small error bars, as in both cases $g = -0.01 \pm 0.02$, which makes this event

a good candidate to host a dark lens (see Section 3.7). Comparison of the χ^2 suggests that the u_0+ solution is preferred, as $\Delta\chi^2 \approx 28$. In addition, the Spitzer-“only” and ground-based-only fits are more compatible for that case (see panels *O* and *P* of the Figure 4).

OGLE-2019-BLG-0169

The Spitzer measurements were only taken at the decline, but close to the peak, which helped to constrain the microlensing parallax from space. They played a significant role in the microlensing parallax determination - see panels *R* and *S*, Figure 4. There is a clear offset between the Spitzer-“only” and all ground-based parallax contours, while the OGLE-only solution is consistent with with Spitzer-“only”. There is a low-level (amplitude of ~ 20 mmag), irregular variability visible in the light curve, which might be the reason for systematic errors in ground-based microlensing parallax measurements. Nonetheless, the final result obtained from the joint fit is driven mostly by the *Spitzer* data, and so is not strongly affected by the systematics in the ground-based data.

In the light curve of OGLE-2019-BLG-0169, at $HJD' \approx 8720$, there is a clear deviation from the light curve model lasting ~ 10 days (see inset of the bottom left panel on Figure 5). It is not an instrumental effect as it appears in both OGLE and KMTNet data. While the scenario of the deviation being a planetary anomaly should not be completely excluded, the amplitude of the variability mentioned in the previous paragraph is comparable to the “anomaly”. Thus, we conduct the analysis using the single lens model and attribute the feature to the variability of the source.

We note that one of the Gaia epochs was taken during the “anomaly”. In an unlikely scenario of the deviation being due to a planet, it might be an interesting point of the analysis of the Gaia astrometric data. The planetary scenario will be investigated elsewhere as it is beyond the scope of this paper.

3.7. Physical parameters - methodology

To assess the probability that the lens is dark, and to provide reasonable predictions of astrometric signal expected from the Gaia mission (see Section 4), we need to estimate the physical properties of the lens, namely its mass, distance and brightness. All the events in the sub-sample analyzed here are standard events with microlensing parallax signal, which means that the light curve does not contain enough information to directly measure these properties. Nonetheless, the microlensing model provides some constraints which, coupled with the assumptions about the Milky Way kinematics and

structure, can be used to evaluate Bayesian probabilities on the physical properties of the lens.

MASS AND DISTANCE

We adopt a similar approach to the one presented in Kruszyńska et al. (2022) and Howil et al. (2024), which in turn is based on the procedure used by Wyrzykowski et al. (2016) and later refined by Mróz & Wyrzykowski (2021). The technical details regarding the Milky Way model are summarized in Mróz & Wyrzykowski (2021) and in the Appendix A of Howil et al. (2024). Below we provide a qualitative description of the analysis and comment on some aspects relevant for our use case.

The starting point of the procedure are posterior distributions of the light curve parameters, obtained from the MCMC modeling. To calculate the mass of the lens, the photometric model has to be supplemented with the source-lens relative proper motion $\mu_{\text{rel}} = |\boldsymbol{\mu}_{\text{rel}}|$. Initially it is drawn from a wide, flat distribution $[0, 30]$ mas/yr and later it is weighted according to the galactic model. Similarly, distance to the source D_s is drawn from a flat distribution $[0, 15]$ kpc. Then, for each link of the MCMC chains resulting from the light curve modeling, we can calculate mass of the lens (see Equation 2) and also its distance, as

$$D_L = \left(\theta_E \pi_E + \frac{1}{D_s} \right)^{-1}, \quad \theta_E = \mu_{\text{rel}} t_E \quad (9)$$

We then apply the “galactic prior” by weighing the resulting mass and distance using weights of the form (Batista et al. 2011):

$$w_{\text{Gal}} = \frac{4}{\text{au}} \frac{D_L^4 \mu_{\text{rel}}^4 t_E}{\pi_E} \nu_d f_\mu f_M M_L. \quad (10)$$

The above expression combine three priors: the mass function f_M , the relative proper motion prior f_μ and stellar density distribution ν_d . Remaining quantities result from the transition between the physical parameters and the microlensing variables. The stellar density distribution ν_d consists of two separate expressions, with “double exponential” disk and barred bulge profiles (see Batista et al. 2011 and Han & Gould 2003). After applying the weights w_{Gal} to lens mass and distance, we obtain the posterior distributions presented in Figure 7.

For the mass function we assume a power law $f_M \sim M^\alpha$, and for each event we address the impact of the assumed mass prior on the final distribution by comparing a “flat” prior $\alpha = -1$ with the Kroupa mass function (Kroupa 2001), where the slope is $\alpha = -2.35$ for the more massive ($M > 0.5 M_\odot$) tail of the distribution (see Table 4). While this is a simplification, as we disregard the different slopes for masses in the range

Table 2. The final (joint ground+space+source color constraint) light curve model fit results for all the events. Most of them have two (u_0+ and u_0-) solutions with comparable χ^2 but for some it was possible to discriminate between them - see more details in the text. **Note.** Blending parameter g is the ratio of the blend flux F_{bl} to the source flux F_{s} . The baseline brightness I_0 is recovered with 1–2 mmag precision in all cases. The photometry error bars are re-normalized, and so $\chi^2/dof \approx 1$ for all the events. Thus, when comparing different models, we use $\Delta\chi^2$ without quoting the number of dof throughout the text.

Event	$t_0 - 2450000$ [days]	u_0	t_E [days]	π_{EN}	π_{EE}	$I_{0,\text{OGLE}}$ [mag]	g_{OGLE}	χ^2/dof
OB150145	$7297.8^{+1.2}_{-1.1}$	$1.13^{+0.26}_{-0.17}$	$76.6^{+8.0}_{-9.5}$	$0.108^{+0.014}_{-0.010}$	$0.111^{+0.020}_{-0.014}$	15.683	$-0.70^{+0.13}_{-0.12}$	668/622
	$7296.9^{+1.1}_{-1.0}$	$-0.62^{+0.05}_{-0.06}$	$116.9^{+5.2}_{-5.5}$	$-0.106^{+0.007}_{-0.007}$	$0.104^{+0.010}_{-0.009}$	15.684	$-0.06^{+0.13}_{-0.13}$	650/622
OB150149	$7277.9^{+0.01}_{-0.01}$	$0.05^{+0.0003}_{-0.0003}$	$101.8^{+0.4}_{-0.4}$	$0.013^{+0.008}_{-0.008}$	$-0.045^{+0.001}_{-0.001}$	15.922	$0.02^{+0.01}_{-0.01}$	1790/1733
	$7277.9^{+0.01}_{-0.01}$	$-0.05^{+0.0003}_{-0.0003}$	$100.8^{+0.4}_{-0.4}$	$0.051^{+0.010}_{-0.010}$	$-0.046^{+0.001}_{-0.001}$	15.922	$0.01^{+0.01}_{-0.01}$	1771/1733
OB150211	$7209.9^{+0.4}_{-0.4}$	$0.65^{+0.09}_{-0.07}$	$95.8^{+7.6}_{-7.9}$	$0.035^{+0.011}_{-0.011}$	$-0.046^{+0.011}_{-0.013}$	17.291	$-0.24^{+0.16}_{-0.15}$	1076/1063
	$7209.5^{+0.4}_{-0.4}$	$-0.64^{+0.07}_{-0.09}$	$96.0^{+7.9}_{-8.0}$	$-0.032^{+0.011}_{-0.012}$	$-0.060^{+0.015}_{-0.018}$	17.291	$-0.21^{+0.16}_{-0.16}$	1078/1063
OB160293	$7669.7^{+0.2}_{-0.2}$	$0.58^{+0.01}_{-0.01}$	$107.3^{+1.2}_{-1.2}$	$0.031^{+0.003}_{-0.003}$	$-0.001^{+0.001}_{-0.001}$	16.223	$-0.11^{+0.03}_{-0.03}$	6096/5959
	$7669.6^{+0.2}_{-0.2}$	$-0.54^{+0.01}_{-0.01}$	$114.3^{+1.4}_{-1.4}$	$-0.037^{+0.003}_{-0.003}$	$-0.006^{+0.001}_{-0.001}$	16.223	$-0.00^{+0.03}_{-0.03}$	6090/5959
OB160689	$7618.7^{+0.3}_{-0.3}$	$1.08^{+0.19}_{-0.13}$	$66.0^{+5.5}_{-6.5}$	$0.142^{+0.034}_{-0.033}$	$-0.048^{+0.011}_{-0.012}$	16.954	$-0.31^{+0.22}_{-0.21}$	3059/3012
	$7618.5^{+0.3}_{-0.3}$	$-0.87^{+0.08}_{-0.10}$	$77.5^{+4.7}_{-4.9}$	$-0.131^{+0.033}_{-0.030}$	$-0.063^{+0.014}_{-0.014}$	16.954	$0.09^{+0.20}_{-0.20}$	3063/3012
OB180410	$8291.8^{+0.01}_{-0.01}$	$0.11^{+0.001}_{-0.001}$	$53.5^{+0.3}_{-0.3}$	$0.052^{+0.021}_{-0.022}$	$0.107^{+0.010}_{-0.011}$	16.567	$-0.02^{+0.01}_{-0.01}$	3599/3490
	$8291.8^{+0.01}_{-0.01}$	$-0.11^{+0.001}_{-0.001}$	$53.0^{+0.3}_{-0.3}$	$-0.136^{+0.022}_{-0.019}$	$0.067^{+0.013}_{-0.014}$	16.567	$-0.03^{+0.01}_{-0.01}$	3580/3490
	$8291.8^{+0.01}_{-0.01}$	$0.11^{+0.0001}_{-0.0001}$	$54.2^{+0.03}_{-0.03}$	$0.015^{+0.019}_{-0.020}$	$0.122^{+0.007}_{-0.007}$	16.567	$-0.00^{+0.00}_{-0.00}$	3607/3490
	$8291.8^{+0.01}_{-0.01}$	$-0.11^{+0.0001}_{-0.0001}$	$54.2^{+0.03}_{-0.03}$	$-0.064^{+0.029}_{-0.023}$	$0.103^{+0.010}_{-0.010}$	16.567	$-0.00^{+0.00}_{-0.00}$	3600/3490
OB180483	$8532.6^{+0.5}_{-0.5}$	$0.16^{+0.01}_{-0.01}$	272.6^{+10}_{-10}	$-0.095^{+0.007}_{-0.007}$	$-0.020^{+0.004}_{-0.004}$	18.584	$-0.15^{+0.05}_{-0.05}$	1170/1225
	$8533.3^{+0.6}_{-0.5}$	$-0.13^{+0.01}_{-0.01}$	328.1^{+11}_{-10}	$0.097^{+0.006}_{-0.006}$	$-0.014^{+0.005}_{-0.005}$	18.586	$0.02^{+0.05}_{-0.05}$	1170/1225
OB180662	$8303.5^{+0.02}_{-0.02}$	$0.26^{+0.004}_{-0.004}$	$65.0^{+0.9}_{-0.8}$	$0.039^{+0.007}_{-0.007}$	$0.040^{+0.003}_{-0.003}$	17.600	$-0.01^{+0.02}_{-0.02}$	2711/2613
	$8303.4^{+0.0}_{-0.0}$	$-0.26^{+0.004}_{-0.004}$	$65.2^{+0.9}_{-0.9}$	$-0.012^{+0.008}_{-0.008}$	$0.043^{+0.006}_{-0.005}$	17.600	$-0.01^{+0.02}_{-0.02}$	2740/2613
OB190169	$8657.9^{+0.1}_{-0.1}$	$0.48^{+0.01}_{-0.01}$	$79.3^{+1.5}_{-1.5}$	$0.005^{+0.006}_{-0.006}$	$-0.045^{+0.006}_{-0.006}$	15.096	$0.13^{+0.05}_{-0.05}$	4799/4637
	$8658.0^{+0.1}_{-0.1}$	$-0.48^{+0.02}_{-0.02}$	$78.9^{+2.0}_{-1.9}$	$-0.085^{+0.012}_{-0.012}$	$-0.054^{+0.011}_{-0.011}$	15.096	$0.13^{+0.06}_{-0.06}$	4768/4637

$M_L < 0.5 M_\odot$, this approach is compatible with the selection process of our sub-sample, which favors more massive lenses. Also, it is a conservative assumption in the context of claims of whether a lens is a dark remnant or not, because the slope of the power law at the massive end is much steeper.

The relative proper motion prior f_μ is constructed based on the lens and source proper motion assumptions. For the lens we consider two distinct cases: the lens lying in the galactic disk and in the bulge. In the first scenario we assume a normal distribution $V_l \approx N(220, 30)$ km/s and $V_b \approx N(0, 20)$ km/s. For the bulge we assume $V_l = V_b \approx N(0, 100)$ km/s (Han & Gould 1995, Batista et al. 2011). These distributions are corrected for the motion of the Sun with respect to the local standard of rest (Schönrich et al. 2010). The mean of the disk velocity distribution also can vary as it depends on the distance to the lens. A more detailed description is outlined in Howil et al. (2024). The phys-

ical velocities of a lens are then transformed to proper motions with $\mu_L = 4.74V_L/D_L$ and after subtraction of the source proper motion (see next paragraph) can be used as a final prior f_μ .

The relative proper motion partially depends on the source proper motion, which is available from Gaia DR3 catalog (Gaia Collaboration et al. 2023), and we incorporate this information in the prior. Values of GDR3 proper motions for each event are presented in Table 3. We also quote the $RUWE^6$ parameter to quantify the credibility of the Gaia measurements. It is important to note that we can use quoted proper motions only for the events where all the light (or at least most of it) actually comes from the source. Otherwise, the proper motion

⁶ Re-normalized Unit Weight Error, see e.g. Gaia Collaboration et al. (2021). Generally, for a well behaved model $RUWE \approx 1$. As a rule of thumb, $RUWE \gtrsim 1.4$ suggests that the astrometric model might not be reliable.

measured by Gaia is a combination of that of the source and blend(s). The majority of events in our sub-sample do not exhibit large blending, and so we decide to include Gaia proper motions in the prior for eight out of nine events. In the remaining case of OGLE-2016-BLG-0689, where the blending appears to be more significant, we use a different approach - see Section 3.8 for more details.

It is also worth noting that the direction of the relative lens-source proper motion can be constrained from the light curve model thanks to the microlensing parallax measurements:

$$\hat{\mu}_{\text{rel}} = \frac{\boldsymbol{\mu}_{\text{rel}}}{\mu_{\text{rel}}} = \frac{\boldsymbol{\pi}_{\text{E}}}{\pi_{\text{E}}}, \quad (11)$$

which has to be taken into account.

In principle, we could assume fixed distance to the source in our calculations - all the events analyzed here lie towards the galactic center, and so it is expected that the sources belong to the bulge population, particularly when their location on the CMD coincides with the Red Clump (see Figure 2). Nonetheless, we decide to weight them with the stellar density distribution, which gives more realistic results. We also decide not to use parallax measurements from GDR3, nor the distance estimates based on them (Bailer-Jones et al. 2021). The reason is that the sources mostly lie in the bulge, and so Gaia parallax is not measured accurately enough (with the signal of the order of ~ 0.1 mas), especially in such crowded fields. Indeed, after inspecting the parallax values quoted in GDR3, we found that the measured parallax is either negative, or `parallax_over_error` $\lesssim 1$, meaning that these measurements do not carry useful information.

It is worth noting that in principle mass and velocity distributions for stellar remnants are different from those of stars. Nonetheless, in this experiment we do not know *a priori* if the lenses belong to the stellar remnant population, and so we cannot assume that from the beginning and use priors for black holes/neutron stars. Instead, we use a Galactic model and the mass function based on stars, and after assessing the amount of light to the lens, we examine the scenario of it being a “regular” star. We note, that if the velocity of a lens is higher, as expected for NSs (e.g. Hobbs et al. 2005) and some BHs (e.g. Repetto et al. 2017), then the derived mass can be regarded as a lower limit⁷.

⁷ It is important to note that in microlensing we access only transverse velocity - the natal-kick velocities of such objects can in principle have any direction and so, due to projection, they will not necessarily be seen as high velocity lenses.

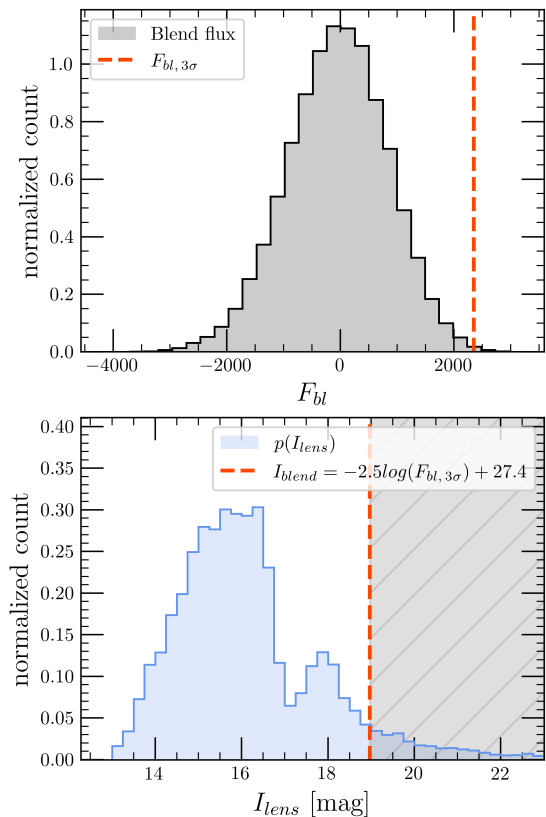


Figure 6. Visualization of the p_{dark} calculation procedure for the example event OGLE-2016-BLG-0293. *Top panel:* posterior distribution of the blend flux (in arbitrary units) resulting from the light curve modeling. Red line shows the blend flux limit we assume for the p_{dark} calculations. *Bottom panel:* posterior distribution $p(I_{\text{lens}})$ of the lens brightness I_{lens} (see details in the text). Red line shows the upper limit on the blend brightness derived from the top histogram. All the samples for which the lens is brighter than the limit (to the left from the red line) contribute to the dark lens scenario.

LENS LIGHT

To claim that a lens is a stellar remnant, not only the mass, but also the blend flux has to be investigated. After constructing the posterior distributions for the lens mass and distance, one can estimate the brightness I_{lens} that the object of these properties should emit, under the assumption that it is a Main Sequence (MS) star. For this purpose we use the empirical mass-luminosity relation found by Pecaut & Mamajek (2013)⁸. If we denote this relation by $L(M_{\text{L}})$, we can define I_{lens} as

$$I_{\text{lens}} = -2.5 \log \frac{L(M_{\text{L}})}{4\pi D_{\text{L}}^2} + A_{\text{lens}}, \quad (12)$$

⁸ <http://www.pas.rochester.edu/~emamajek>

Table 3. Positions, proper motions and $RUWE$ (see footnote 6) parameters for all the events in the analyzed sample, taken from the GDR3 catalog. In the last two columns we also provide the alert name, for those detected through Gaia Science Alerts (GSA), and the GDR3 source identifier.

Event	RA (J2016)	Dec (J2016)	μ_{RA^*} [mas/yr]	μ_{Dec} [mas/yr]	$RUWE$	GSA name	GDR3 source_id
OB150145	270.17782	-35.15408	-1.29 ± 0.07	-6.51 ± 0.05	1.03	-	4041998223399082752
OB150149	270.28819	-32.55773	-2.01 ± 0.21	-5.03 ± 0.13	2.35	-	4042928139682133120
OB150211	262.35909	-30.98178	-3.50 ± 0.29	-7.22 ± 0.21	1.05	-	4058004814930630912
OB160293	268.16140	-32.48960	-1.49 ± 0.09	-7.48 ± 0.07	0.92	-	4043504794840743040
OB160689	261.14944	-30.13245	-1.80 ± 0.36	-7.25 ± 0.23	1.38	-	4059051309459806208
OB180410	272.22770	-27.16974	-4.51 ± 0.16	-6.84 ± 0.11	1.14	Gaia18cho	4063011505688647296
OB180483	262.64177	-27.49183	4.85 ± 1.23	-2.13 ± 0.74	1.34	Gaia18ayh	4061439448723558016
OB180662	266.87754	-32.52442	-5.74 ± 0.59	-6.09 ± 0.34	1.13	Gaia18cej	4054012488194100096
OB190169	265.98559	-32.87095	-0.87 ± 0.11	-4.54 ± 0.06	0.97	Gaia19drv	4054032245075925760

where A_{lens} is extinction to the lens.

To estimate A_{lens} , we use extinction maps from Nataf et al. (2013) for the 4 events lying in the OGLE-III fields covered in their analysis. For the remaining five events we derive the extinction value based on the Red Clump position on the CMD, using similar procedure as Nataf et al., using their de-reddened RC brightness. The A_{lens} parameter is the extinction integrated along the whole distance to the source, so we treat it as an upper limit on the lens extinction. Again, for the sake of claiming if the lens is a stellar remnant or not, this is a conservative assumption. In addition, this simplification is justified by the fact that most of the disk dust between the observer and the source resides within the first few kiloparsecs from Earth, especially for the events with larger galactic latitudes.

Having a distribution of I_{lens} , one can compare it with the brightness of the blend, which is one of the products of the light curve modeling. In the case where the total blend brightness is higher than I_{lens} , we get more light from the blend than is expected from the lens of given mass at a given distance. Such scenario is very common and easy to explain, as the excess can be attributed to any other sources lying on the same line of sight and not participating in microlensing - the lens is not the only light source contributing to the blending light, which is common for the galactic bulge direction. On the other hand, if the blend brightness calculated from the photometric model is lower than I_{lens} , the situation is opposite - there is not enough light emitted by the blend to explain a MS star of given mass at given distance. In other words, such MS star would be too bright

compared to the expected blend light⁹. It suggests that the lensing object is in fact not luminous. Then, if it is massive enough, it is considered a candidate for a stellar remnant.

To perform the comparison between I_{lens} and blend brightness, the latter has to be estimated based on the blend flux distribution F_{bl} , that is the product of the light curve modeling. To be conservative, we choose a $3\text{-}\sigma$ upper limit on the blend flux (red dashed line on the top panel of Figure 6). To compare it with I_{lens} we translate this limit to magnitudes and call it I_{blend} (red dashed line on the bottom panel of Figure 6).

As mentioned above, the lens is expected to be dark for each set of parameters (each link of MCMC chains) resulting in $I_{lens} < I_{blend}$. To formally assess the probability p_{dark} that the lens is dark, we integrate all the samples for which $I_{lens} < I_{blend}$:

$$p_{dark} = \frac{\int_0^{I_{blend}} p(I_{lens}) dI_{lens}}{\int_{-\infty}^{\infty} p(I_{lens}) dI_{lens}}, \quad (13)$$

where $p(I_{lens})$ is the posterior distribution of the I_{lens} brightness. We illustrate this procedure on the Figure 6: all the samples for which lens brightness can be explained by the blend are grayed-out on the bottom panel. For the remaining part of the distribution, the lens with given mass at given distance would be too bright to explain it with a MS star, and thus this region corresponds to the dark lens scenario.

3.8. Physical parameters - results

Below we provide results of the Bayesian analysis for each event separately.

⁹ We treat MS stars as a reference in this analysis, but more evolved star of given mass would be even brighter

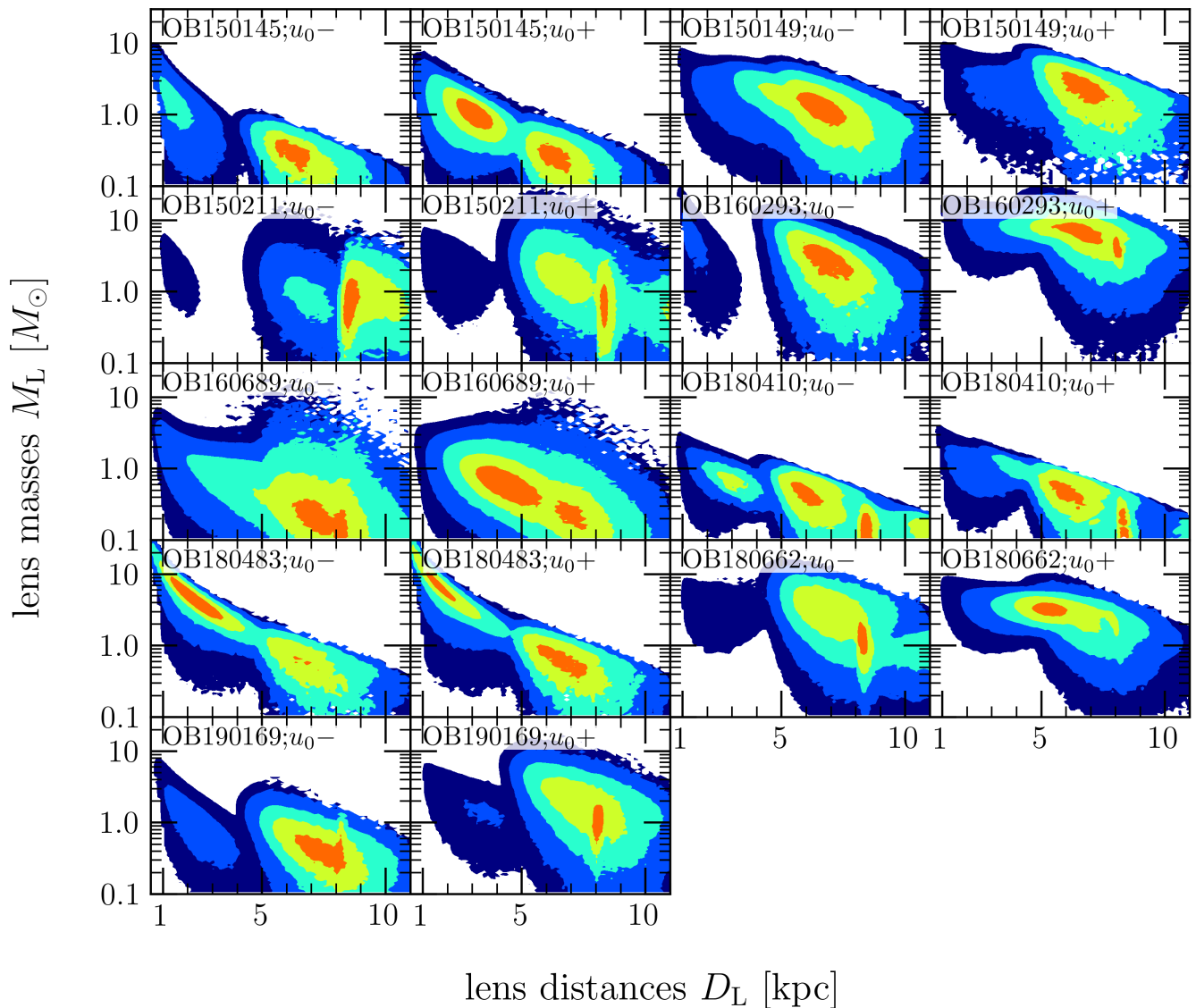


Figure 7. Posterior distributions for lens mass and distance, under the assumption of the Kroupa mass function (slope $\alpha = -2.35$) – see text for the details. The orange, yellow, cyan, blue and dark blue contours mark 1,2,3,4 and 5- σ confidence levels, respectively. Note, that we show the distributions for all the possible solutions (both u_0+ and u_0- models for each event), even though some of them can be rejected based on the light curve analysis. We list the results for preferred solutions in Table 4.

OGLE-2015-BLG-0145

In the Figure 7 we present the Bayesian analysis results for both the u_0- and u_0+ solutions, although the u_0+ one is virtually excluded by the light curve analysis (see Section 3.6). The M_L vs D_L distribution shows a bi-modality as lens is either in the disk or in the bulge. This overall structure is visible in most of the events in the sub-sample, although usually a bulge lens

is the preferred solution, as expected. Indeed, for the u_0- solution here, the bulge scenario is much more preferred and it yields a low lens mass $M_L = 0.30^{+0.17}_{-0.12}$ at $D_L = 6.12^{+0.87}_{-0.75}$, with very low chance of being dark (see Table 4).

OGLE-2015-BLG-0149

In the $M_L - D_L$ plane, the two solutions behave in a similar way, with only one maximum each. The pre-

Table 4. Results of Bayesian analysis in the form of median values of marginalized distributions for lens masses, distances and Einstein radii, along with the probabilities that the lens is dark. The error values reflect the 68% confidence level intervals. We also show the $2\text{-}\sigma$ lower limit on the lens mass $M_{L,2\sigma\text{min}}$. For each event we show the more preferred solution (either u_0+ or u_0-) and results for the two priors on the mass function (see text for more information.)

Event	Model	Mass prior	Lens mass M_L [M_\odot]	$M_{L,2\sigma\text{min}}$ [M_\odot]	Lens distance D_L [kpc]	θ_E [mas]	p_{dark}
OB150145	u_0-	Flat	$0.83^{+3.49}_{-0.53}$	0.17	$2.14^{+4.17}_{-1.38}$	$1.00^{+4.26}_{-0.63}$	49.9%
	u_0-	Kroupa MF	$0.30^{+0.17}_{-0.12}$	0.09	$6.15^{+0.83}_{-0.77}$	$0.36^{+0.19}_{-0.14}$	5.8%
OB150149	u_0-	Flat	$1.80^{+0.83}_{-0.64}$	0.70	$6.00^{+0.93}_{-1.14}$	$0.97^{+0.42}_{-0.32}$	92.5%
	u_0-	Kroupa MF	$1.40^{+0.75}_{-0.56}$	0.45	$6.35^{+0.95}_{-0.29}$	$0.77^{+0.38}_{-0.29}$	79.0%
OB150211	u_0+	Flat	$2.74^{+3.35}_{-1.65}$	0.56	$6.80^{+1.47}_{-1.07}$	$1.05^{+0.72}_{-0.61}$	28.4%
	u_0+	Kroupa MF	$1.04^{+1.41}_{-0.49}$	0.30	$8.20^{+0.17}_{-1.75}$	$0.43^{+0.57}_{-0.16}$	4.7%
OB160293	u_0-	Flat	$4.02^{+1.86}_{-1.48}$	1.46	$6.23^{+0.86}_{-0.70}$	$1.21^{+0.54}_{-0.44}$	98.9%
	u_0-	Kroupa MF	$2.98^{+1.75}_{-1.28}$	0.85	$6.58^{+0.91}_{-0.80}$	$0.91^{+0.52}_{-0.39}$	93.6%
OB160689	u_0+	Flat	$1.10^{+0.79}_{-0.48}$	0.31	$4.00^{+1.60}_{-1.00}$	$1.11^{+0.50}_{-0.42}$	42.2%
	u_0+	Kroupa MF	$0.68^{+0.54}_{-0.36}$	0.13	$4.48^{+2.10}_{-1.19}$	$0.79^{+0.48}_{-0.40}$	16.2%
OB180410	u_0-	Flat	$0.58^{+0.24}_{-0.21}$	0.16	$5.62^{+0.89}_{-2.53}$	$0.59^{+0.45}_{-0.22}$	-
	u_0-	Kroupa MF	$0.42^{+0.24}_{-0.26}$	0.08	$6.09^{+2.23}_{-0.91}$	$0.42^{+0.30}_{-0.25}$	-
OB180483	u_0-	Flat	$6.82^{+5.56}_{-2.63}$	2.55	$1.55^{+0.71}_{-0.62}$	$5.35^{+4.34}_{-2.04}$	99.6%
	u_0-	Kroupa MF	$4.65^{+3.12}_{-2.08}$	0.47	$2.07^{+1.03}_{-0.69}$	$3.68^{+2.42}_{-1.62}$	92.3%
OB180662	u_0+	Flat	$3.33^{+0.65}_{-0.60}$	2.02	$5.28^{+0.80}_{-0.66}$	$1.48^{+0.25}_{-0.23}$	99.9%
	u_0+	Kroupa MF	$3.15^{+0.66}_{-0.64}$	1.54	$5.35^{+0.95}_{-0.67}$	$1.42^{+0.25}_{-0.26}$	99.3%
OB190169	u_0-	Flat	$0.71^{+0.41}_{-0.28}$	0.25	$6.63^{+1.26}_{-0.91}$	$0.54^{+0.25}_{-0.20}$	0.7%
	u_0-	Kroupa MF	$0.50^{+0.32}_{-0.22}$	0.15	$7.12^{+1.01}_{-1.03}$	$0.40^{+0.22}_{-0.17}$	0.1%

ferred u_0- solution places the lens at around 6.3 kpc with mass in the range $0.7 - 2 M_\odot$. The 79% probability of being dark suggests that the lens might be a massive white dwarf or a neutron star. This is the only event in the sample that has *RUWE* parameter value substantially higher than one (see Table 3) and so we decided to perform the Bayesian analysis with the source proper motion prior (taken from GDR3 and thus, given high *RUWE*, unreliable) loosened. Nominally we use $1\text{-}\sigma$ value from GDR3 as a width of the prior. Here we are broadening the prior to ten standard deviations, as the Gaia values should not be fully trusted. We do not observe significant change in the $M_L - D_L$ plane, apart from the anticipated broadening of the posterior distributions.

OGLE-2015-BLG-0211

The $M_L - D_L$ plane is again similar for the two solutions, with only the bulge lens scenario being viable. In both distributions one can see an additional, sharper structure at around 8 kpc. Loosening the Gaia prior makes it merge with the wider bulge distribution, which means it is caused by the source proper motion prior.

Similar structure is visible in some of the other events in the sub-sample.

OGLE-2016-BLG-0293

The lens in this event is one of the best candidates for a massive remnant in the analyzed sub-sample. Multiple factors in the light curve modeling suggest that the u_0- model is correct (see 3.6) and so we present values yielded by this model in Table 4.

Although θ_E does not have extreme value, thanks to a small microlensing parallax, the resulting lens mass is somewhat large and is expected to lie in the range $1.7 - 4.9 M_\odot$ for bulge lenses. This results in a 94% probability for the lens being dark. Hence, it is an excellent candidate for a neutron star or a stellar mass black hole. There is a possibility that the lens lies in the disk, which yields even higher masses, but it is strongly disfavored in our analysis (see relevant panel in Figure 7).

OGLE-2016-BLG-0689

The blending for this event is not well constrained from the photometric model, but is likely non-negligible (see Section 3.6). As a result, the proper motion de-

tected by Gaia is a combination of source and lens proper motion, which means that we can not use it directly in the prior as source proper motion. Instead, when calculating the prior on relative proper motion, we assume the source proper motion to be $(\mu_l, \mu_b) = (-6.12, -0.19) \pm 2.64 \text{ mas/yr}$ Schönrich et al. (2010). This corresponds to a typical motion of the galactic center relative to the Sun and is a reasonable assumption as the source most likely resides in the bulge. The same procedure was applied in Mroz et al. (2021). Naturally, the resulting M_L vs D_L distribution is much wider compared to the one resulting from the approach with the Gaia value. Because of the low expected lens mass and presumably strong blending, it is very unlikely that this event hosts a remnant lens.

OGLE-2018-BLG-0410

The u_0- solution is preferred in terms of goodness of fit in the light curve analysis ($\Delta\chi^2 \approx 19$). Redoing the photometric fit with the blending fixed to zero helps to resolve part of the tension between the microlensing parallax solutions (see Section 3.6), and so we use this model to estimate the physical parameters. With the blending parameter fixed to zero we can not assess the probability of the lens to be dark, as it is assumed to be dark in the first place. Nonetheless, the mass of the lens yielded by our analysis is very low, and so it is most likely an ordinary dwarf star lying in the bulge.

OGLE-2018-BLG-0483

There is a clear bi-modality in the M_L vs D_L distribution due to the duality in the possible lens populations. Each of the u_0+ and u_0- solutions have the disk lens solution, in which the lens is relatively heavy, in the range $5 - 10 M_\odot$, and bulge lens solution where $M_L \lesssim 1 M_\odot$. The u_0+ case is excluded with the flux Spitzer limits, so we know u_0- the correct one. From the posterior distribution of the lens mass and distance for the negative solution, it seems that the scenario of heavier lens located in the disk is more preferred, although there is a small region of similar probability for the bulge lens case. As the blending is very low for this event, the lens is a good remnant candidate with estimated mass $M_L = 4.65_{-2.08}^{+3.12}$ and $p_{\text{dark}} \approx 92\%$.

OGLE-2018-BLG-0662

The positive solution is favored both in terms of goodness of fit and compatibility of ground-based-only and Spitzer-“only” parallax solutions (see section 3.6). The expected mass for this event remains somewhat large for a range of lens distances (see Figure 7). Additionally, the blending level is very low, which makes this event

one of the best candidates in our sub-sample to host a dark remnant with $M_L = 3.15 \pm 0.65$ and $p_{\text{dark}} \approx 99\%$.

OGLE-2019-BLG-0169

In the $M_L - D_L$ plane, in both of the solutions we can see the impact of the GDR3 source proper motion prior, similarly to OGLE-2015-BLG-0211 - the narrow structure gradually disappears with the increase of the width of the prior. None of the solutions shows the prospect for the remnant lens, and the preferred u_0- case suggests particularly low probability for that with mass of the lens $M_L \approx 0.5 M_\odot$ and $p_{\text{dark}} < 1\%$.

4. GAIA PREDICTIONS

All the events analyzed here were chosen under the condition that they had been observed by the Gaia mission and so there will be high precision astrometry available for them in the Gaia Data Release 4 (GDR4, to be published ~ 2026). Knowing the epochs of astrometric measurements, the expected uncertainties and assuming θ_E values derived in Section 3.7, we perform realistic simulations of the Gaia astrometry and investigate the prospects for measuring θ_E and consequently the masses of the lenses in the studied events.

The Gaia mission will provide 2D astrometry only for the brightest objects ($G > 13$ mag). For the remaining ones, only one-dimensional astrometry, measured along the instantaneous scanning direction \hat{AL} , which we will denote with angle ψ measured from the North direction eastward. In the simulations, we use actual values of scanning angles and epochs calculated based on the Gaia scanning law, taken from GOST¹⁰ (Gaia Observation and Forecast Tool). We treat each Gaia visit as a single epoch, without dividing into sub-measurements from each AF (Astrometric Field)¹¹. To estimate the error bars, we follow the conservative approach of Rybicki et al. (2018), where the centroiding errors from de Bruijne et al. (2014) are increased by 50% to account for potential systematics. They also take into consideration the fact that there are measurements from multiple AFs within one epoch, which scales down the error bars by a factor of $\sqrt{9} = 3$.

CENTROID TRAJECTORY MODEL

The shift of the centroid position from the position of the source can be expressed as (e.g. Dominik & Sahu 2000)

$$\delta = \frac{\mathbf{u}}{u^2 + 2} \theta_E. \quad (14)$$

¹⁰ <https://gaia.esac.esa.int/gost/>

¹¹ Gaia constantly rotates, and so whenever an object is observed, it transits the focal plane, passing through (nominally) 9 AFs.

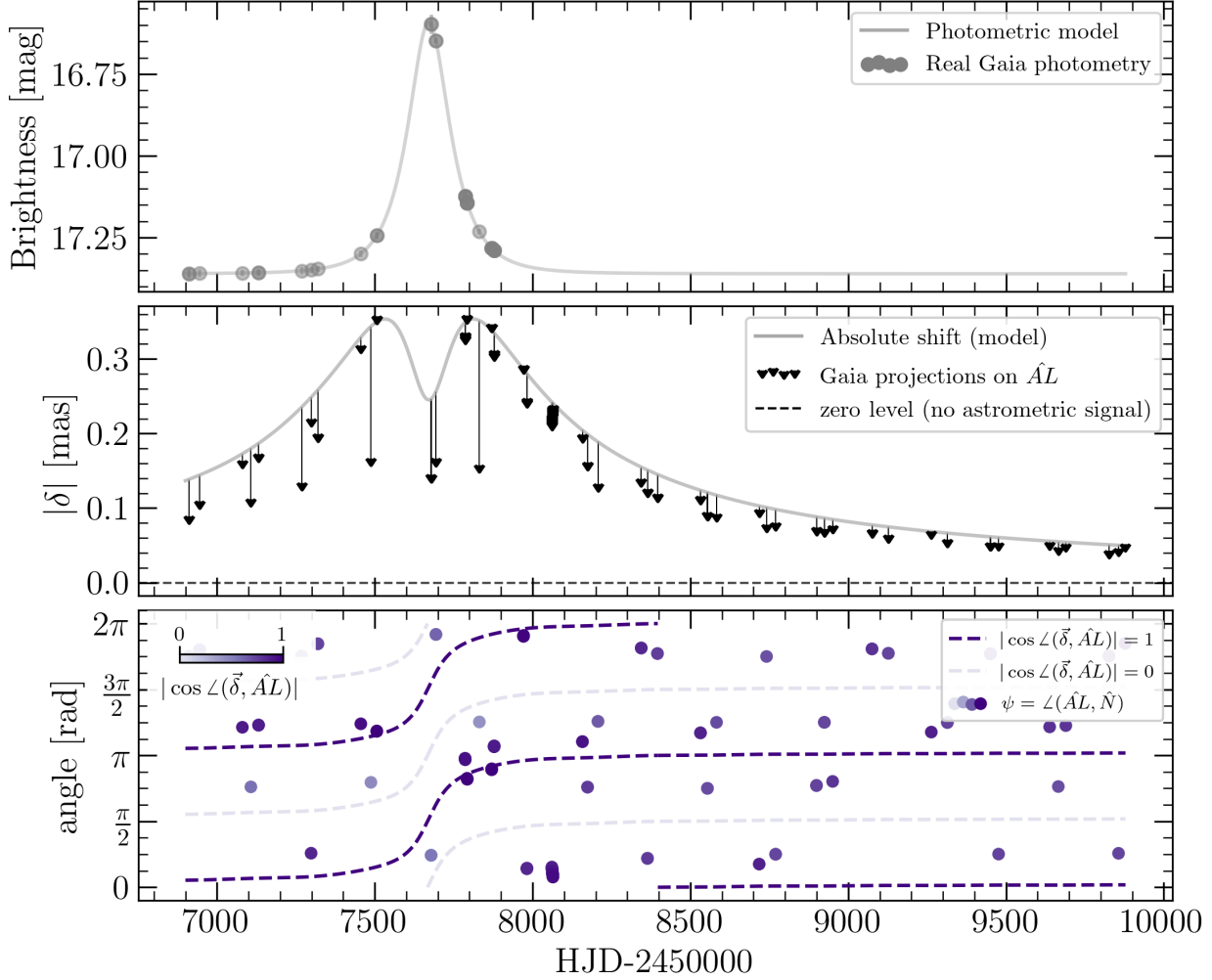


Figure 8. Visualization of all the known information about the Gaia measurements, under the assumption of the photometric microlensing model and $\theta_E = 0.91$ mas (see Table 4), for the case of OGLE-2016-BLG-0293. *Top panel:* Photometric model with marked Gaia measurements. *Middle panel:* Absolute astrometric shift calculated based on the photometric model (gray line). The black arrows indicate how much the astrometric signal is “reduced” due to the projection on the \widehat{AL} direction. *Bottom panel:* Points represent scanning angles of Gaia mission for this field. Dark dashed lines show the direction of the astrometric shift vector $\delta \pm 180^\circ$, while light-colored dashed lines mark perpendicular directions. Gaia only provides measurements along the instantaneous scanning direction \widehat{AL} . As a result, whenever astrometric shift vector δ and \widehat{AL} are aligned or counter-aligned ($|\cos \angle(\delta, \widehat{AL})| \approx 1$), the signal measured by Gaia is larger. This occurs when the points on the bottom panel are darker and situated closer to one of the dark lines. Indeed, one can see that darker points on the bottom panel correspond to shorter arrows on the middle panel, meaning that more astrometric signal is “available” for Gaia.

Because we are investigating the Gaia potential to detect the astrometric microlensing effect, for now we disregard the source proper motion and parallax. In simulated data they will be easily distinguished from the microlensing and thus, to first order, should not affect how well the microlensing signal can be recovered. On the other hand, while dealing with the real data, potentially contaminated by unknown systematics, a full model with parallax and proper motions will have to be applied.

Based on the Equation 14, one can see that information about the astrometric shift comes from three somewhat distinct instances: the relative separation $u(t)$, the direction of the lens-source relative motion, and the Einstein radius. The first is almost always available as the relative separation is a function of parameters easily derivable from the standard light curve, namely (t_0, u_0, t_E) . It means that, for all standard events that are relatively well covered, one can already predict the astrometric shift of the centroid for each solution (which traces out an ellipse, see e.g. Dominik & Sahu 2000 for details), although without orienting it on the sky or scaling it to the absolute angular units. For events considered in this analysis, we also have very strong constraints on the microlensing parallax vector, which in turn gives the direction of the lens-source relative proper motion (see Equation 11). In consequence, we are able to align the centroid shift trajectory on the sky only using the light curve model. As a result, for each photometric solution, the only information that needs to be recovered from the astrometric data is θ_E – the scaling factor of the microlensing ellipse, whose shape and orientation are already known. It leads to the conclusion, that even astrometric data of seemingly insufficient precision, might provide enough information to determine the Einstein radius.

To construct the model of the astrometric microlensing shift as seen by *Gaia*, one has to project the vector $\boldsymbol{\delta} = (\delta_N, \delta_E)$ onto the scan direction \widehat{AL} , and so the one-dimensional astrometric microlensing signal observed by the satellite can be written as:

$$\delta_\psi = \boldsymbol{\delta} \cdot \widehat{AL} = \delta_N \cos \psi + \delta_E \sin \psi. \quad (15)$$

In the Figure 8, we visualize the “transition” from the two-dimensional signal to the one-dimensional Gaia data. The absolute astrometric microlensing shift presented in the middle panel (gray continuous line) is “reduced” by the projection on the \widehat{AL} direction, which is denoted by arrows. The level of this reduction depends on the angle between the astrometric shift and the scanning direction, which changes in time, as shown on the bottom panel of the figure.

We use posterior distributions on the physical parameters derived in Section 3.7 to calculate θ_E and generate 1-D Gaia astrometry for all the events in the sub-sample.

4.1. Detectability

To quantify the detectability of astrometric microlensing, we first simulate the Gaia data, following steps and assumptions from the previous subsection. Then we calculate the χ^2 statistic for the “null-model”, which is the case where astrometric microlensing is not present (effectively $\theta_E = 0$):

$$\chi_{\text{null}}^2 = \sum_i \frac{(\delta_{\psi,i} - \delta_{\psi,0,i})^2}{\sigma_i^2}, \quad (16)$$

where the sum is evaluated over all Gaia measurements and σ_i are their respective uncertainties. Because we only consider the astrometric signal from microlensing, our null-model is simply the baseline level and thus $\delta_{\psi,0} = 0$. Finally, calculating the difference $\Delta\chi^2 = \chi_{\text{null}}^2 - \chi^2$, between the χ^2 of the null-model and the correct model with astrometric microlensing, allows us to evaluate the confidence level for detecting the astrometric signal present in the Gaia data.

In the top panel of the Figure 9, we show an example of one-dimensional astrometric Gaia data for OGLE-2016-BLG-0293, simulated with realistic scatter. As mentioned before, the only information that we need to extract from the astrometry is θ_E – a scaling factor of the model whose shape is already known for a given set of photometric parameters. Thus, even though the visual inspection of the top panel of the Figure 9 does not reveal any obvious signal, the bottom panel with the cumulative $\Delta\chi^2$ plot shows that (for event OGLE-2016-BLG-0293) the astrometric signal should be strong enough to detect it.

4.2. Results

For all the events in the sub-sample, we assess the detectability of the astrometric microlensing signatures by comparing the null model to the model generated with the microlensing signal, as explained in the previous section. Two events require some caution in interpreting the results though. The first one is OGLE-2016-BLG-0689, which is likely blended. Then, the signal measured by Gaia is a combination of the flux from the source and lens/blend(s). As a consequence, the astrometric microlensing signal expected here will be much weaker and the measurement much less robust. The second event is OGLE-2015-BLG-0149. In that case the *RUWE* parameter is notably larger than unity, which suggests that the Gaia 5-parameter astrometric solution can be unreliable. As a result, the real Gaia data for

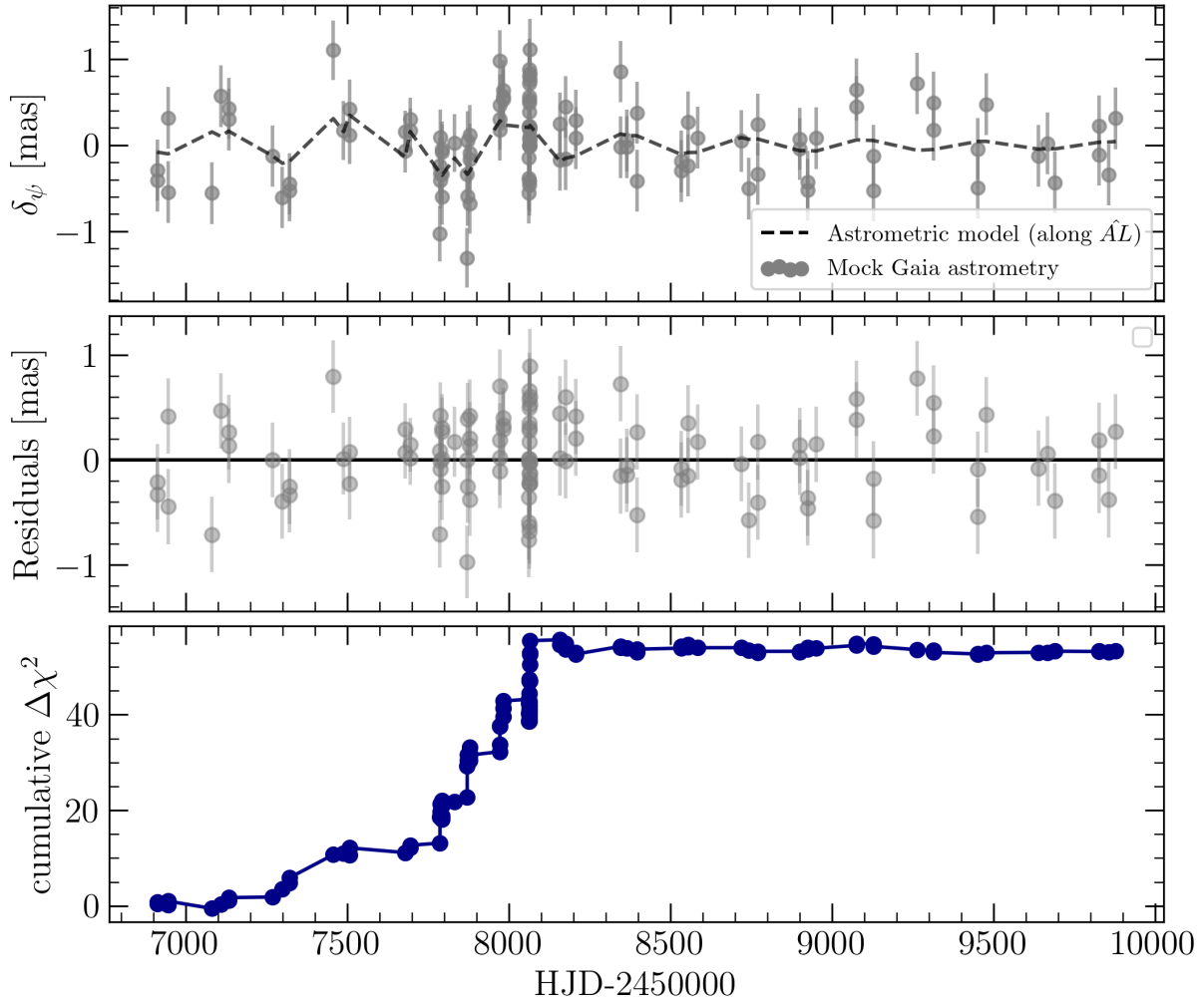


Figure 9. The cumulative plot of $\Delta\chi^2$ of the astrometric 1-D fit for the event OGLE-2016-BLG-0293 for an example realization of the Gaia data and $\theta_E = 0.91$ mas (see Table 4). *Top panel:* Mock Gaia astrometry (gray points) of the centroid displacement during microlensing (proper motion and parallax not included here). Model used to generate the data is marked by the dashed line. *Middle panel:* Residuals of the data and the model shown on the top panel. *Bottom panel:* Cumulative $\Delta\chi^2$, which is the difference between the null model and the astrometric microlensing model (see details in the text).

this event might look different than what we simulate here and so the measurement of astrometric microlensing signal may be more difficult.

We simulate the Gaia data and calculate $\Delta\chi^2$ for the nine events, using θ_E values range spanning from 0.1 to 5 milliarcseconds, to construct a relation between θ_E and $\Delta\chi^2$. Having statistical estimates of the lens masses and Einstein radii, presented in Section 3.7, we are able to use this relation to determine for which events we expect to detect the astrometric microlensing signal in the Gaia data. The results are presented in Figure 10,

where we show the relations between $\Delta\chi^2$ and Einstein radius, also marking the θ_E values that are expected from the Bayesian analysis (see Table 4). Out of the nine analyzed events, two of them show promising results in terms of Gaia astrometry detection capabilities: OGLE-2016-BLG-0293 (magenta marker on Figure 10) and OGLE-2018-BLG-0483 (black). The difference between the astrometric null model and the microlensing model for the two events is $\Delta\chi_{\text{OB160293}}^2 \approx 35$ and $\Delta\chi_{\text{OB180483}}^2 \approx 24$. Taking into account the one-parameter difference between the null-model and mi-

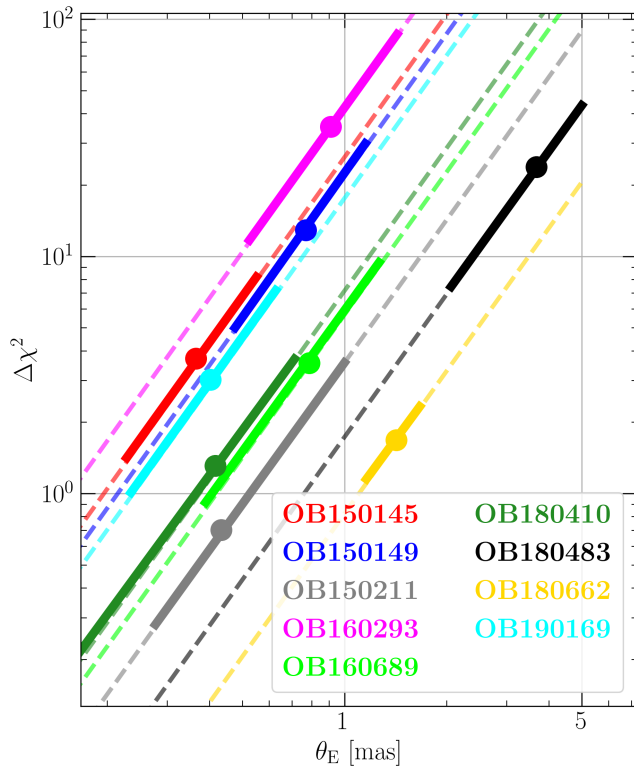


Figure 10. Detectability of the astrometric microlensing in Gaia data for the selected sub-sample of long timescale Spitzer events, plotted as a function of Einstein radius θ_E . The $\Delta\chi^2$ parameter is the difference between the null model and the best-fit astrometric microlensing model (see details in the text). Points represent expected θ_E values for each event that were calculated in Section 3.7 and listed in Table 4. Thickened lines mark $1-\sigma$ errors on θ_E . We also simulated Gaia astrometric data for wider range of Einstein radii - the detectability for θ_E in range from 0.1 to 5 mas is plotted with dashed lines.

microlensing model (one dof difference), it translates to about $6-\sigma$ and $5-\sigma$ expected detection level, respectively.

Generally, there are multiple factors impacting the detectability of the astrometric microlensing signal in the Gaia data. The most important ones are the Einstein radius, the brightness of the event, Gaia sampling and the scanning angles configuration. It is not a surprise that the two events mentioned above are preferred. In the case of OGLE-2016-BLG-0293 all of the above requirements are met - in addition to the relatively large predicted $\theta_E = 0.91$ mas and several points covering the amplified part of the light curve, the event is bright having $I_{0,OGLE} = 16.2$ mag. The latter is particularly important, because Gaia astrometric accuracy declines steeply with decrease in brightness. On the other hand, OGLE-2018-BLG-0483 is faint with baseline at $I_{0,OGLE} \approx 18.6$

mag (and even fainter in *Gaia* as $I_{0,Gaia} \approx 20.0$ mag), but we expect it to be detected in the Gaia data thanks to its extreme time scale $t_E \approx 330$ days, which translates into a large Einstein radius. Another favorable consequence of the long timescale is the fact that there are more data points from Gaia throughout the (significantly) amplified part of the light curve, which further enhanced detectability.

The second group consists of four events that are less likely to be detected, with the expected astrometric signal on the level of $1.5-3\sigma$: OGLE-2015-BLG-0145 (red marker on Figure 10), OGLE-2015-BLG-0149 (dark blue), OGLE-2019-BLG-0169 (cyan), and OGLE-2016-BLG-0689 (light green). The events from this group are bright and relatively long (see Table 2), but according to our mass/distance analysis, the most probable Einstein radius values for favored solutions are likely too small to be robustly detected by Gaia, even for such bright targets. The OGLE-2015-BLG-0149 event stands out here, but as already mentioned, it is more challenging to make predictions for due to the higher $RUWE$ value.

In the case of OGLE-2015-BLG-0211 (gray) and OGLE-2018-BLG-0410 (green) the expected detectability is even smaller, with the astrometric microlensing signal at or below the $1-\sigma$ level. The reason is that the Einstein radii are rather small ($\theta_E \lesssim 0.5$ mas) and these events are fainter than the three targets mentioned before.

Finally, the mass measurement of the lens in the OGLE-2018-BLG-0662 (yellow) event is also rather unlikely through the detection of astrometric microlensing in the Gaia data, even though the expected lens mass and Einstein radius are large (see Table 4). In this case, the main factors affecting the detectability prospects are the relatively low brightness of the event ($I_{0,OGLE} = 17.6$; additionally the source is very red, meaning the brightness in G -band is significantly lower) and duration of the event - even though the relatively short timescale $t_E = 66.6$ days translates to a somewhat large Einstein radius $\theta_E = 1.47$ mas, it results in fewer Gaia data points covering the event. Moreover, the scanning angle configuration is such that the 1-D astrometric signal is close to zero for a large fraction of the few important points. As a consequence, one of the best black hole candidates in our sample, with an expected dark lens of mass $2.5-4.2 M_\odot$ is unlikely to be confirmed by the Gaia astrometry.

5. SUMMARY AND CONCLUSIONS

In this work, we analyzed a sub-sample of nine events chosen from the whole population of microlensing events observed by the *Spitzer* Space Telescope in the years

2014-2019. The sub-sample was chosen from the events that had been also observed by the *Gaia* mission, with long time scales and small microlensing parallaxes. The last two requirements were used to identify candidates for massive lenses.

Based on this small sub-sample, we demonstrate the procedures that will be applied to the whole *Spitzer* sample of microlensing events, which will allow us to populate $t_E - \pi_E$ diagram and conduct statistical analysis of microlensing parallax. Such analysis is necessary to complete the studies on the planets frequency in the Galaxy, which is based on microlensing planets detected in the *Spitzer* campaign.

The detailed analysis of the selected sub-sample of nine events allowed us to identify candidates for black holes and neutron stars that can be later confirmed by the *Gaia* time-series astrometry, which is expected to be released in the early 2026. Based on the Bayesian analysis incorporating the Galactic model and proper motion information from GDR3 (Section 3.7) we found four candidates for dark remnant lenses: OGLE-2016-BLG-0293, OGLE-2018-BLG-0483, OGLE-2018-BLG-0662 and OGLE-2015-BLG-0149 (see Table 4 for estimated masses). The masses of the lenses of the four candidate events lie somewhat on the edge of the known distinction between the neutron stars and stellar black holes. In the case of OGLE-2015-BLG-0149 it is most likely a neutron star. As for the remaining three candidates, the median mass suggests black holes, although the error bars are large and so the heavy neutron star scenario can not be excluded. The cases of OGLE-2016-BLG-0293 and OGLE-2018-BLG-0483 are expected to have an astrometric microlensing signal detectable by *Gaia*, which in turn will allow to confirm the mass of the lens and their remnant nature.

1 E.O.O. is grateful for the support of grants from the
 2 Willner Family Leadership Institute, André Deloro In-
 3 stitute, Paul and Tina Gardner, The Norman E Alexan-
 4 der Family M Foundation ULTRASAT Data Center
 5 Fund, Israel Science Foundation, Israeli Ministry of Sci-
 6 ence, Minerva, NSF-BSF, Israel Council for Higher Edu-
 7 cation (VATAT), Sagol Weizmann-MIT, Yeda-Sela, and
 8 the Rosa and Emilio Segre Research Award. This re-
 9 search was supported by the Institute for Environmental
 10 Sustainability (IES) and The André Deloro Institute for
 11 Space and Optics Research at the Weizmann Institute
 12 of Science.

13 This research has made use of the KMTNet system op-
 14 erated by the Korea Astronomy and Space Science Insti-
 15 tute (KASI) at three host sites of CTIO in Chile, SAAO
 16 in South Africa, and SSO in Australia. Data transfer
 17 from the host site to KASI was supported by the Korea
 18 Research Environment Open NETwork (KREONET).
 19 This research was supported by KASI under the R&D
 20 program (project No. 2024-1-832-01) supervised by
 21 the Ministry of Science and ICT. W.Zang, H.Y., S.M.,
 22 R.K., J.Z., and W.Zhu acknowledge support by the Na-
 23 tional Natural Science Foundation of China (Grant No.
 24 12133005). W.Zang acknowledges the support from the
 25 Harvard-Smithsonian Center for Astrophysics through
 26 the CfA Fellowship. J.C.Y. and I.-G.S. acknowledge
 27 support from U.S. NSF Grant No. AST-2108414. Y.S.
 28 acknowledges support from BSF Grant No. 2020740.
 29 Work by C.H. was supported by the grants of National
 30 Research Foundation of Korea (2019R1A2C2085965 and
 31 2020R1A4A2002885).

32 The MOA project is supported by JSPS KAKENHI
 33 Grant Number JP24253004, JP26247023, JP16H06287
 34 and JP22H00153.

ACKNOWLEDGEMENTS

REFERENCES

- Abbott, B. P., Abbott, R., Abbott, T. D., et al. 2016, *Physical Review Letters*, 116, 061102, doi: [10.1103/PhysRevLett.116.061102](https://doi.org/10.1103/PhysRevLett.116.061102)
- Bachelet, E., Norbury, M., Bozza, V., & Street, R. 2017, *AJ*, 154, 203, doi: [10.3847/1538-3881/aa911c](https://doi.org/10.3847/1538-3881/aa911c)
- Bachelet, E., Zieliński, P., Gromadzki, M., et al. 2022, *A&A*, 657, A17, doi: [10.1051/0004-6361/202039548](https://doi.org/10.1051/0004-6361/202039548)
- Bailer-Jones, C. A. L., Rybizki, J., Fouesneau, M., Demleitner, M., & Andrae, R. 2021, *AJ*, 161, 147, doi: [10.3847/1538-3881/abd806](https://doi.org/10.3847/1538-3881/abd806)
- Batista, V., Gould, A., Dieters, S., et al. 2011, *A&A*, 529, A102, doi: [10.1051/0004-6361/201016111](https://doi.org/10.1051/0004-6361/201016111)
- Bond, I. A., Abe, F., Dodd, R. J., et al. 2001, *MNRAS*, 327, 868, doi: [10.1046/j.1365-8711.2001.04776.x](https://doi.org/10.1046/j.1365-8711.2001.04776.x)
- Bozza, V., Bachelet, E., Bartolić, F., et al. 2018, *MNRAS*, 479, 5157, doi: [10.1093/mnras/sty1791](https://doi.org/10.1093/mnras/sty1791)
- Calchi Novati, S., Gould, A., Udalski, A., et al. 2015, *ApJ*, 804, 20, doi: [10.1088/0004-637X/804/1/20](https://doi.org/10.1088/0004-637X/804/1/20)
- Cassan, A., & Ranc, C. 2016, *MNRAS*, 458, 2074, doi: [10.1093/mnras/stw372](https://doi.org/10.1093/mnras/stw372)
- Cassan, A., Ranc, C., Absil, O., et al. 2022, *Nature Astronomy*, 6, 121, doi: [10.1038/s41550-021-01514-w](https://doi.org/10.1038/s41550-021-01514-w)
- de Bruijne, J. H. J., Rygl, K. L. J., & Antoja, T. 2014, in *EAS Publications Series*, Vol. 67, EAS Publications Series, 23–29, doi: [10.1051/eas/1567004](https://doi.org/10.1051/eas/1567004)
- Delplancke, F., Górski, K. M., & Richichi, A. 2001, *A&A*, 375, 701, doi: [10.1051/0004-6361:20010783](https://doi.org/10.1051/0004-6361:20010783)
- DePoy, D. L., Atwood, B., Belville, S. R., et al. 2003, in *Society of Photo-Optical Instrumentation Engineers (SPIE) Conference Series*, Vol. 4841, *Instrument Design and Performance for Optical/Infrared Ground-based Telescopes*, ed. M. Iye & A. F. M. Moorwood, 827–838, doi: [10.1117/12.459907](https://doi.org/10.1117/12.459907)
- Dominik, M., & Sahu, K. C. 2000, *ApJ*, 534, 213, doi: [10.1086/308716](https://doi.org/10.1086/308716)
- Evans, D. W., Riello, M., De Angeli, F., et al. 2018, *A&A*, 616, A4, doi: [10.1051/0004-6361/201832756](https://doi.org/10.1051/0004-6361/201832756)
- Fardeen, J., McGill, P., Perkins, S. E., et al. 2024, *ApJ*, 965, 138, doi: [10.3847/1538-4357/ad3243](https://doi.org/10.3847/1538-4357/ad3243)
- Fukui, A., Suzuki, D., Koshimoto, N., et al. 2019, *AJ*, 158, 206, doi: [10.3847/1538-3881/ab487f](https://doi.org/10.3847/1538-3881/ab487f)
- Gaia Collaboration, Prusti, T., de Bruijne, J. H. J., et al. 2016, *A&A*, 595, A1, doi: [10.1051/0004-6361/201629272](https://doi.org/10.1051/0004-6361/201629272)
- Gaia Collaboration, Brown, A. G. A., Vallenari, A., et al. 2021, *A&A*, 649, A1, doi: [10.1051/0004-6361/202039657](https://doi.org/10.1051/0004-6361/202039657)
- Gaia Collaboration, Vallenari, A., Brown, A. G. A., et al. 2023, *A&A*, 674, A1, doi: [10.1051/0004-6361/202243940](https://doi.org/10.1051/0004-6361/202243940)
- Gould, A. 1994, *ApJL*, 421, L75, doi: [10.1086/187191](https://doi.org/10.1086/187191)
- . 2004, *ApJ*, 606, 319, doi: [10.1086/382782](https://doi.org/10.1086/382782)
- . 2019, *Journal of Korean Astronomical Society*, 52, 121, doi: [10.5303/JKAS.2019.52.4.121](https://doi.org/10.5303/JKAS.2019.52.4.121)
- . 2023, arXiv e-prints, arXiv:2310.19164, doi: [10.48550/arXiv.2310.19164](https://doi.org/10.48550/arXiv.2310.19164)
- Gould, A., Ryu, Y.-H., Calchi Novati, S., et al. 2020, *Journal of Korean Astronomical Society*, 53, 9, <https://arxiv.org/abs/1906.11183>
- Gravity+ Collaboration, Abuter, R., Alarcon, P., et al. 2022, *The Messenger*, 189, 17, doi: [10.18727/0722-6691/5285](https://doi.org/10.18727/0722-6691/5285)
- Han, C., & Gould, A. 1995, *ApJ*, 449, 521, doi: [10.1086/176076](https://doi.org/10.1086/176076)
- . 2003, *ApJ*, 592, 172, doi: [10.1086/375706](https://doi.org/10.1086/375706)
- Hobbs, G., Lorimer, D. R., Lyne, A. G., & Kramer, M. 2005, *MNRAS*, 360, 974, doi: [10.1111/j.1365-2966.2005.09087.x](https://doi.org/10.1111/j.1365-2966.2005.09087.x)
- Hodgkin, S. T., Wyrzykowski, L., Blagorodnova, N., & Koposov, S. 2013, *Philosophical Transactions of the Royal Society of London Series A*, 371, 20120239, doi: [10.1098/rsta.2012.0239](https://doi.org/10.1098/rsta.2012.0239)
- Hodgkin, S. T., Harrison, D. L., Breedt, E., et al. 2021, *A&A*, 652, A76, doi: [10.1051/0004-6361/202140735](https://doi.org/10.1051/0004-6361/202140735)
- Howil, K., Wyrzykowski, L., Kruszyńska, K., et al. 2024, arXiv e-prints, arXiv:2403.09006, doi: [10.48550/arXiv.2403.09006](https://doi.org/10.48550/arXiv.2403.09006)
- Kim, S.-L., Lee, C.-U., Park, B.-G., et al. 2016, *Journal of Korean Astronomical Society*, 49, 37, doi: [10.5303/JKAS.2016.49.1.037](https://doi.org/10.5303/JKAS.2016.49.1.037)
- Klüter, J., Bastian, U., & Wambsganss, J. 2020, *A&A*, 640, A83, doi: [10.1051/0004-6361/201937061](https://doi.org/10.1051/0004-6361/201937061)
- Kroupa, P. 2001, *MNRAS*, 322, 231, doi: [10.1046/j.1365-8711.2001.04022.x](https://doi.org/10.1046/j.1365-8711.2001.04022.x)
- Kruszyńska, K., Wyrzykowski, L., Rybicki, K. A., et al. 2022, *A&A*, 662, A59, doi: [10.1051/0004-6361/202142602](https://doi.org/10.1051/0004-6361/202142602)
- Lam, C. Y., & Lu, J. R. 2023, *ApJ*, 955, 116, doi: [10.3847/1538-4357/aced4a](https://doi.org/10.3847/1538-4357/aced4a)
- Lam, C. Y., Lu, J. R., Udalski, A., et al. 2022, *ApJL*, 933, L23, doi: [10.3847/2041-8213/ac7442](https://doi.org/10.3847/2041-8213/ac7442)
- Lu, J. R., Sinukoff, E., Ofek, E. O., Udalski, A., & Kozłowski, S. 2016, *ApJ*, 830, 41, doi: [10.3847/0004-637X/830/1/41](https://doi.org/10.3847/0004-637X/830/1/41)
- McGill, P., Anderson, J., Casertano, S., et al. 2023, *MNRAS*, 520, 259, doi: [10.1093/mnras/stac3532](https://doi.org/10.1093/mnras/stac3532)
- Mróz, P., Udalski, A., & Gould, A. 2022, *ApJL*, 937, L24, doi: [10.3847/2041-8213/ac90bb](https://doi.org/10.3847/2041-8213/ac90bb)
- Mroz, P., Udalski, A., Wyrzykowski, L., et al. 2021, arXiv e-prints, arXiv:2107.13697, doi: [10.48550/arXiv.2107.13697](https://doi.org/10.48550/arXiv.2107.13697)

- Mróz, P., & Wyrzykowski, L. 2021, *AcA*, 71, 89, doi: [10.32023/0001-5237/71.2.1](https://doi.org/10.32023/0001-5237/71.2.1)
- Nataf, D. M., Gould, A., Fouqué, P., et al. 2013, *ApJ*, 769, 88, doi: [10.1088/0004-637X/769/2/88](https://doi.org/10.1088/0004-637X/769/2/88)
- Nucita, A. A., Licchelli, D., De Paolis, F., et al. 2018, *MNRAS*, 476, 2962, doi: [10.1093/mnras/sty448](https://doi.org/10.1093/mnras/sty448)
- Paczynski, B. 1986, *ApJ*, 304, 1, doi: [10.1086/164140](https://doi.org/10.1086/164140)
- Pecaut, M. J., & Mamajek, E. E. 2013, *ApJS*, 208, 9, doi: [10.1088/0067-0049/208/1/9](https://doi.org/10.1088/0067-0049/208/1/9)
- Refsdal, S. 1966, *MNRAS*, 134, 315, doi: [10.1093/mnras/134.3.315](https://doi.org/10.1093/mnras/134.3.315)
- Repetto, S., Igoshev, A. P., & Nelemans, G. 2017, *MNRAS*, 467, 298, doi: [10.1093/mnras/stx027](https://doi.org/10.1093/mnras/stx027)
- Rybicki, K. A., Wyrzykowski, L., Klencki, J., et al. 2018, *MNRAS*, 476, 2013, doi: [10.1093/mnras/sty356](https://doi.org/10.1093/mnras/sty356)
- Rybicki, K. A., Wyrzykowski, L., Bachelet, E., et al. 2022, *A&A*, 657, A18, doi: [10.1051/0004-6361/202039542](https://doi.org/10.1051/0004-6361/202039542)
- Sahu, K. C., Anderson, J., Casertano, S., et al. 2017, *Science*, 356, 1046, doi: [10.1126/science.aal2879](https://doi.org/10.1126/science.aal2879)
- . 2022, *ApJ*, 933, 83, doi: [10.3847/1538-4357/ac739e](https://doi.org/10.3847/1538-4357/ac739e)
- Sajadian, S., & Sahu, K. C. 2023, *AJ*, 165, 96, doi: [10.3847/1538-3881/acb20f](https://doi.org/10.3847/1538-3881/acb20f)
- Schönrich, R., Binney, J., & Dehnen, W. 2010, *MNRAS*, 403, 1829, doi: [10.1111/j.1365-2966.2010.16253.x](https://doi.org/10.1111/j.1365-2966.2010.16253.x)
- Udalski, A., Szymanski, M., Kaluzny, J., Kubiak, M., & Mateo, M. 1992, *AcA*, 42, 253
- Udalski, A., Szymański, M. K., & Szymański, G. 2015a, *AcA*, 65, 1. <https://arxiv.org/abs/1504.05966>
- Udalski, A., Yee, J. C., Gould, A., et al. 2015b, *ApJ*, 799, 237, doi: [10.1088/0004-637X/799/2/237](https://doi.org/10.1088/0004-637X/799/2/237)
- Wozniak, P. R. 2000, *AcA*, 50, 421
- Wyrzykowski, L., & Mandel, I. 2020, *A&A*, 636, A20, doi: [10.1051/0004-6361/201935842](https://doi.org/10.1051/0004-6361/201935842)
- Wyrzykowski, L., Kostrzewa-Rutkowska, Z., Skowron, J., et al. 2016, *MNRAS*, 458, 3012, doi: [10.1093/mnras/stw426](https://doi.org/10.1093/mnras/stw426)
- Wyrzykowski, L., Kruszyńska, K., Rybicki, K. A., et al. 2023, *A&A*, 674, A23, doi: [10.1051/0004-6361/202243756](https://doi.org/10.1051/0004-6361/202243756)
- Yee, J. C., Shvartzvald, Y., Gal-Yam, A., et al. 2012, *ApJ*, 755, 102, doi: [10.1088/0004-637X/755/2/102](https://doi.org/10.1088/0004-637X/755/2/102)
- Yee, J. C., Udalski, A., Calchi Novati, S., et al. 2015, *ApJ*, 802, 76, doi: [10.1088/0004-637X/802/2/76](https://doi.org/10.1088/0004-637X/802/2/76)
- Zang, W., Dong, S., Gould, A., et al. 2020, *ApJ*, 897, 180, doi: [10.3847/1538-4357/ab9749](https://doi.org/10.3847/1538-4357/ab9749)
- Zurlo, A., Gratton, R., Mesa, D., et al. 2018, *MNRAS*, 480, 236, doi: [10.1093/mnras/sty1805](https://doi.org/10.1093/mnras/sty1805)